Universidad de Concepción
Dirección de Postgrado
Facultad de Ciencias Físicas y Matemáticas
Programa de Doctorado en Ciencias Físicas

BÚSQUEDA DE TRÁNSITOS EXOPLANETARIOS EN EL BULBO GALÁCTICO

(SEARCH FOR EXOPLANETARY TRANSITS IN THE GALACTIC BULGE)

Tesis para optar al grado de Doctor en Ciencias Físicas

Caddy Coral Cortés Orellana
Concepción - Chile
Enero 2019

Profesor Guía: Dr. Dante Minniti
Profesor Co-Guía: Dr. Sandro Villanova
Departamento de Astronomía
Facultad de Ciencias Físicas y Matemáticas
Universidad de Concepción

Agradecimientos

Quiero agradecer a mis tutores Prof. Dante Minniti y Prof. Sandro Villanova por ser parte importante en mi formación, por apoyarme en mi investigación y por ayudarme a llegar a esta etapa final de mi Doctorado.

Además, me gustaría agradecer a mi pololo Cesar por brindarme su constante apoyo y por motivarme a seguir adelante, sin duda esto no podría haber sido posible sin ti. Desde mi ciudad natal, Arica, siempre he recibido un gran apoyo de mi familia. A pesar de la distancia, han estado presente, es por eso que todo mi trabajo es gracias a ustedes. Me gustaría también agradecer a mis amigos, por brindarme su amistad que ha perdurado en el tiempo. También me gustaría agradecer a mi pequeña tortuga Kepler. Él ha estado conmigo 10 años, siempre acompañandome en las largas noches de estudio, tu gran cariño me da tranquilidad y fuerza para seguir.

Finalmente, quiero agradecer a CONICYT, ya que esta investigación no podría haber sido posible sin el financiamiento de CONICYT-PCHA/Doctorado Nacional/2014-21141084.

Resumen

Contexto: El Bulbo es la componente de nuestra Galaxia más antigua. Por ende, es esencial estudiar diferentes objetos en el Bulbo Galáctico, para entender la formación y evolución de la Vía Láctea.

Objetivos: Nuestro principal objetivo es detectar y estudiar nuevos planetas extrasolares en el Bulbo Galáctico. Posteriormente, nosotros encontraremos los parámetros estelares y planetarios, para poder caracterizar los exoplanetas encontrados.

Metodología: Mediante el método de tránsito nosotros buscaremos planetas extrasolares usando los datos de la misión K2, de la campaña 9 y 11. Nosotros calcularemos un periodrama Box Least Squares, para detectar una señal periodica. Luego de este proceso, nosotros realizamos una inspección visual para descartar falsos positivos. Además, aprovecharemos los datos del infrarrojo cercano del VVV survey que se superponen con los datos de K2, para descartar falsos positivos, especialmente objetos que se combinan.

Resultados: Nosotros reportamos el descubrimiento de cinco exoplanetas candidatos detectados en el Bulbo Galáctico. Dos de estos candidatos podrían ser planetas de baja masa y tres de ellos podrían ser gigantes gaseosos. Gracias al VVV survey, nosotros buscaremos la variabilidad de las estrellas pertenecientes a los cúmulos globulares del bulbo NGC 6528, NGC 6553 y NGC 6569, los cuales son parte del estudio de Muñoz et al. (2018) y Muñoz et al., (2019, en preparación). Encontrando en cada uno de ellos una estrella variable candidata.

Abstract

Context: The Bulge is the oldest component of our Galaxy. Therefore, it is essential to study different objects in the Galactic Bulge, to understand the formation and evolution of the Milky Way.

Aims: Our main goal is to detect and study new extrasolar planets in the Galactic Bulge. Later, we determine the stellar and planetary parameters, in order to characterize the exoplanets found.

Methods: Through the transit method we search for extrasolar planets using the K2 database from campaigns 9 and 11. We calculate a Box Least Squares periodogram, to detect a periodic signal. After this process, we perform a visual inspection to discard obvious false positives. Additionally, we take advantage of the near-infrared data from the VVV survey that overlapped with the K2 data, to discard false positives, specially blended object.

Results: We report the discovery of five exoplanet candidates detected in the Galactic Bulge, two of which could be low mass planets, and three could be giants gaseous planets. Thanks to the VVV survey, we search for variability in stars belonging to the Bulge Globular Clusters: NGC 6528, NGC 6553 and NGC 6569, which are part of the study of Muñoz et al. (2018) and Muñoz et al. (2019, in preparation). We detected in each of the globular clusters one candidate variable star.

Contents

List of Tables

List of Figures

1

Introduction

Our Galaxy is a spiral galaxy mainly composed of three parts: the bulge, the disk and the halo. Also, we can find different types of stars, which can be classified according to the metallicity content. These can be divided into three types: population I stars have large metallicities, population II stars have relatively low metallicities and the population III stars theoretically have zero metallicity. These populations are distributed throughout the Milky Way, so the disk is composed of both, population I and II stars while the halo contains population II stars. In addition, we can observe a variety of astronomical objects in these populations. For instance, the high metallicity of Population I stars makes them more likely to contain planetary systems that the other two populations, because the metallicity plays an important role in planet formation (Buchhave et al., 2014). The population II stars, have a spherical distribution. Globular clusters for example are typical representatives of population II stars. Presumably, the center of the globular cluster distribution is the center of the galaxy. For this, we need to find the distances to the clusters and a good distance indicator are the variable stars as Cepheids and RR Lyrae.

In this thesis, we study different objects in the galactic bulge. We are searching for extrasolar planets. That is possible, because the K2 mission in 2016 observed for the first time the center the Milky Way during the campaign 9, in order to study gravitational microlensing events. At the end of that year, K2 observed the bulge again with the campaign

11, collecting a total of approximately 15.000 light curves. We take advantage of the high-precision photometry of the K2 database to search for exoplanets, finding five exoplanet candidates (see Caption 2), two of which could be low mass planets, and three could be giant gaseous planets. Thank to the multi-band near-IR photometry of the VVV survey and 2MASS we can measure accurate physical parameters for the host stars. With the VVV survey also we can obtain multi-epoch observations in K_s band, which is very useful for studying variable stars. For this reason, we search for variability in three Bulge Globular Clusters: NGC 6528, NGC 6553 and NGC 6569. These clusters were part of the study of chemical characterization using high-resolution spectroscopy from FLAMES-UVES. Muñoz et al. (2018) and Muñoz et al. (2019, in preparation) analyzed stars on the red giant branch and obtained chemical abundances of light elements, iron-peak elements, α elements, and heavy elements. We search for variability in these stars, and we detected in each of the globular clusters one candidate variable star (see Caption 3).

1.1 Exoplanet Detection Techniques

Different methods have been developed for the detection of extrasolar planets: radial velocity, astrometry, microlensing, transit, and direct imaging. The figure 1.1, show that these methods are based on two principles: indirect methods, which measure the influence that the planet causes on its host star and the direct methods, that detect the signals that come directly from the planet. Each of these techniques have observational incompleteness, as shown in Figure 1.2 the radial velocity and transit methods detect planets preferentially that orbit closer to their host stars, and these planets are larger in mass and size. In another hand, the planets detected with microlensing, astrometry, and direct imaging have larger orbital distances. There are so far 3903 planets confirmed with these methods in 2909 systems, with 647 systems that have more than one planet. Although the thesis was focussed on the science and usage of the transit method, in this section we describe the different detection techniques.

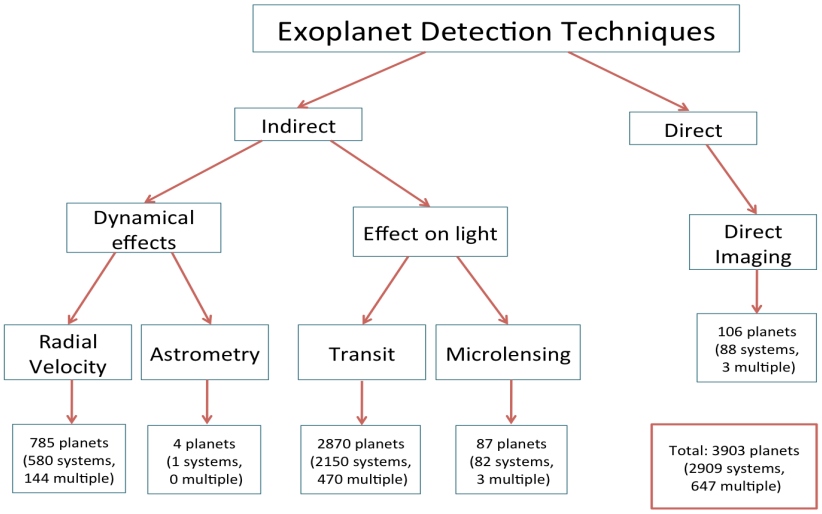

Figure 1.1 Detection methods for exoplanets. The data is taken from exoplanet.eu. Source: Own elaboration.

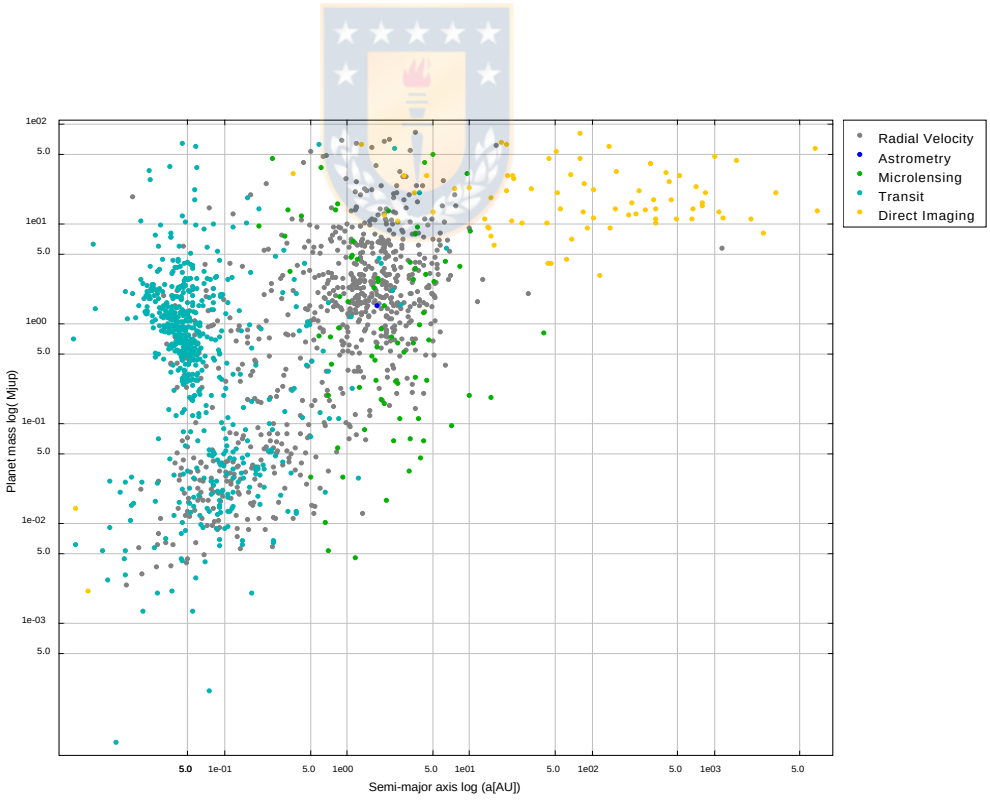

Figure 1.2 Planetary mass vs. semi-axis major. The different colors shows the method used to detect the planet. The data is taken from exoplanet.eu. Source: Own elaboration.

1.1.1 Radial Velocity

The radial velocity method or Doppler spectroscopy is an indirect method, that is used to measure the gravitational influence that an orbiting planet induces on a star. This technique was implemented by Campbell et al. (1988) finding evidence that the binary system γ Cephei has a very low mass companion of 1.7 M_J, which was later confirmed by Hatzes et al. (2003). After finding the first exoplanet Pegasi 51 b (Mayor & Queloz, 1995) with radial velocity method and thanks to the improvement of the Doppler precision, with this method there are 785 exoplanets discovered so far.

Using the Doppler effect it is possible to measure the variation of the projected velocity. The method consists (see Figure 1.3) in the measurement of the wavelength of emitted light from a source when this is moving toward the observer (blueshift) and when it is moving away (redshift). The measured radial velocity of the star, V_r is represented by

$$V_r(t) = K[\cos(\omega + v(t)) + e\cos(\omega)] \tag{1.1}$$

where ω is the longitude of periastron, e the eccentricity, v(t) the angle used to characterize an observational orbit and for definition, the radial velocity semi-amplitude of the sinusoidal oscillation (K) is:

$$K \equiv \frac{2\pi}{P}\frac{a_\star \sin i}{(1-e^2)^{1/2}} \tag{1.2}$$

where G is the universal gravitational ($6.67x10^{-11}[m^3Kg^{-1}s^{-2}]$), P is the orbital period, $a_\star$ is the semi-major axis of the stellar orbit around the system barycenter and i is the inclination of the orbit plane. An alternative expression for this equation without $a_\star$ is described by Cumming et al. (1999), Eq. (1):

$$K = \left(\frac{2\pi G}{P}\right)^{1/3}\frac{M_p \sin i}{(M_p + M_\star)^{2/3}}\frac{1}{\sqrt{1-e^2}} \tag{1.3}$$

where M_p is the planetary mass and $M_\star$ is the stellar mass.

For a circular orbit with $M_p \ll M_\star$, the stellar velocity variations are sinusoidal with amplitude (Cumming et al. 1999, Eq. 2):

$$K = 28.4 m s^{-1} \left(\frac{P}{1yr}\right)^{-1/3} \left(\frac{M_p \sin i}{M_J}\right) \left(\frac{M_\star}{M_\odot}\right)^{-2/3} \tag{1.4}$$

With the observational parameters: velocity semi-amplitude (K), orbital period (P) and eccentricity (e), it is possible calculate a minimum of the planet mass ($M_p \sin i$) with the stellar mass ($M_\star$) previously determined. It is not possible to determine the true planetary mass, because of the inclination of the orbit is unknown.

The radial velocity has an observational bias. It is for this reason that the majority of the detected planets have high masses and short orbital distances, for example: one of the exoplanets with the shortest period detected is EPIC 248435473 b (Rodriguez et al., 2018) with P= 0.6585 days and the most massive is HD 87883 b (Fischer et al., 2009) with M=81.9 M_J.

One of the observational parameters that we obtained from the radial velocity is the eccentricity, for example: the planet with highest eccentricity e=0.92 is HD 20782 b (Jones et al., 2006) and has a=1.36 AU and the exoplanet with circular orbit is HD 156668 b (Donnison, 2010) with a=0.05 AU. There is a relationship between the eccentricity and the semi-major axis, therefore the planets with circular orbits are closer to their host star, while planets with a large eccentricities are farther away.

To search exoplanets with the radial velocity method there are different spectrographs, some of them are: CORALIE (Queloz et al., 2001) installed at 1.2m "Leownard Euler" Swiss Telescope with precision 3 m/s, HARPS (Mayor et al., 2003) at the Silla 3.6m telescope with a precision 1 m/s and ESPRESSO (Pepe et al., 2010) mounted on the ESO VLT with a precision < 10 cm/s.

1.1.2 Astrometry

The astrometry technique is an indirect method that measures the changes of the position of the star on the sky because of the gravitational influence of the companion.

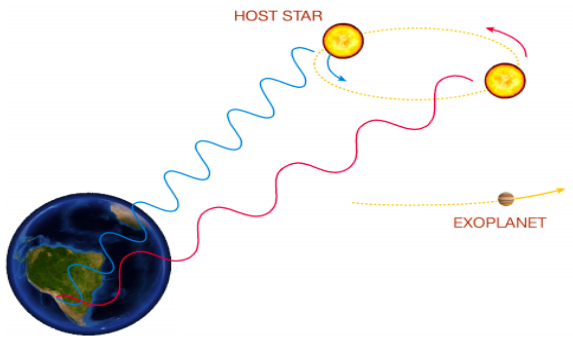

Figure 1.3 Radial Velocity scheme described the blueshift when the star moves towards us and the redshift when it moves away from us. Source: European Southern Observatory (ESO).

The path of a star orbiting the star-planet barycenter appears projected on the plane of the sky as an ellipse with angular semi-major axis α given by

$$\alpha = \frac{M_p a}{M_\star d} \tag{1.5}$$

where a is the semi-major axis of the planet orbit, d is the distance, and M_p and $M_\star$ are the mass of the planet and the star, respectively. According to this equation, the astrometric method is sensitive to detect high mass planets and large orbits.

Figure 1.4 shows the astrometric signature that the planets of the solar system produce on a solar-like star located at 10 pc, therefore a very high precision is necessary to find an extrasolar planet. We can deduce that is difficult to find exoplanets through astrometry, and for this reason, there are few exoplanets discovered by this technique (see Figure 1.1). Another difficulty is the turbulence in the Earth's atmosphere when we perform observations from the ground, although it can be reduced (Lazorenko & Lazorenko, 2004; Cameron et al., 2009; Shao & Colavita, 1992). The space astrometry avoids the effect of the Earth's atmosphere and improves the precision of the astrometric measurement.

Figure 1.4 shows the astrometric precision for three missions: the Hipparcos satellite that operated between 1989 to 1992 measured the position, proper motions and direct distances for more than 100.000 stars with a precision of 1 milli-arcsecond (Perryman

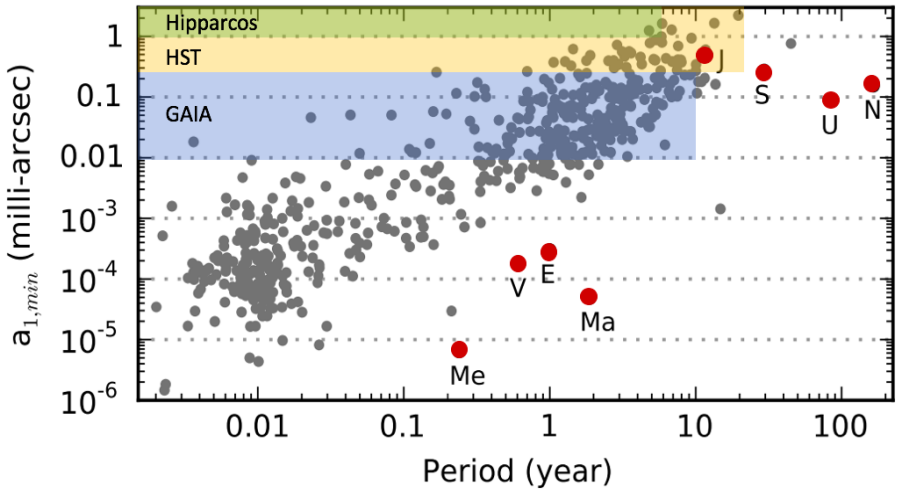

Figure 1.4 Minimum astrometric signature vs orbital period. The grey circles represent 570 planets discovered with other techniques. The red circles are a reference of the astrometric signature that the solar system planets cause on a solar-like star at 10 pc. The green, yellow and blue areas show the precision of the Hipparcos, HST and GAIA missions, respectively. Source: From Eduardo Bendek (Meeting ExoPAG10[1]) adapted from Fischer et al. (2014).

et al., 1997), HST has a precision of 0.25 milli-arcsecond (McArthur et al., 2010) and the Gaia satellite which is mapping a billion of stars with a precision of 0.01 milli-arcsecond.

1.1.3 Microlensing

Microlensing is an indirect method, which occurs when two stars are aligned and the gravitational field of a star acts like a lens, magnifying the light of a distant background star. Although the majority of the exoplanets found with this method have a large mass (see Figure 1.2), as is the case of OGLE-2016-BLG-0693L b with M = 49 M_J (Ryu et al., 2017), this technique is more sensitive than others to detect small planets. The first planet found was OGLE 2003-BLG-235/MOA 2003-BLG-53 with M = 2.6 M_J (Bond et al., 2004) in 2003 by the OGLE and MOA survey. The Figure 1.5 represents the geometry of a microlensig event. From the source star (S) the light is bent by the lens star (L),

[1]https://exoplanets.nasa.gov/exep/events/13/exopag-10/

therefore the observer (O) sees the image (I) of the source instead of the truth. When the source is perfectly aligned with the lens and the observer, it produces a ring known as Einstein ring, whose radius is described as:

$$r_E = \Theta_E D_L = \left[\frac{4GM_L}{c^2} \frac{D_S - D_L}{D_S} \right]^{1/2} \tag{1.6}$$

where Θ_E is the angular Einstein radius, D_S is the source distance, D_L is the lens distance and M_L is the lens mass. During a microlensing event, the brightness of the source is amplified by

$$A = \frac{u^2 + 2}{u(u^2 + 4)^{1/2}} \tag{1.7}$$

where u is the angular separation between the lens and the source in units of the Einstein radius. If the observer, the lens and the source are aligned, $u = 0$ and $A = \infty$. Thus, the point of infinite magnification is known as caustic. When the source crosses a caustic produced by the planet, it is possible to detect the planet. One advantage of this technique, is that it is the only method capable of detecting planets in other galaxies (Dai & Guerras, 2018).

Different surveys have been used to detect exoplanets, for example, OGLE project (Udalski et al., 1992), for which the main goal is to study microlensing events in the Magellanic Clouds and the Galactic bulge, due to a large number of background stars that are potential targets for microlensing. For their development, a telescope was constructed (1.3 m Warsaw Telescope) located in the Campanas Observatory. MOA (Bond et al., 2001) is another project focussed in observing dark matter, exoplanets and stellar atmospheres using the microlensing technique, with a 1.8m reflector telescope. The Korea Microlensing Telescope Network (KMTNet, Park et al. 2012) projects focus is to discover exoplanets, principally earth-mass planets in the habitable zone with the gravitational microlensing technique. This project consists of three telescopes located at: SAAO, CTIO, and SSO.

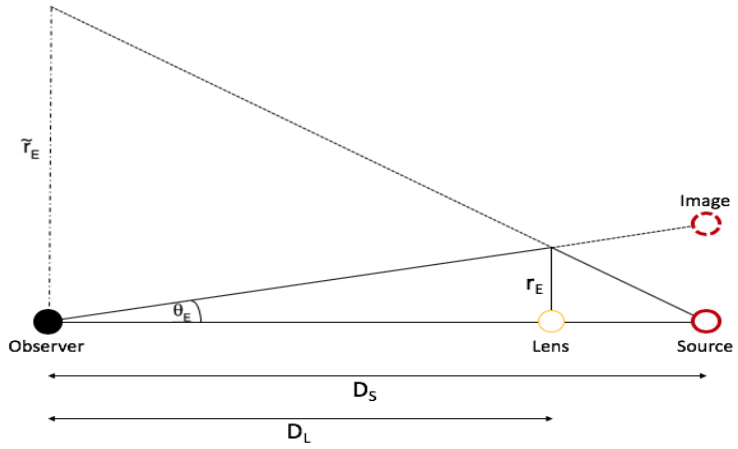

Figure 1.5 Schematized geometry of microlensing. Source: Own elaboration.

1.1.4 Transit

When a planet crosses in front of a host star, it blocks some of the star light during the eclipse (transit) and creates a periodic drop in the brightness of the star. This definition is represented in Figure 1.6, where the dashed lines show the first to the fourth contact points, ΔF is the transit depth, $t_{transit}$ is the transit duration between the first and fourth contact and t_{flat} is the duration of the flat part of the transit, in the interval between the second and third contact. Through this method it is possible to determine the planetary radius, semi-major axis and the inclination (see Section 1.2.1). The first exoplanet discovered with this method was HD 209458 b (Henry et al., 1999; Charbonneau et al., 2000) with a radius of 1.38 R_J and a semi-major axis of 0.0475 AU. Since then, with this method 2870 planets have been discovered. Despite the large number of exoplanets found, we only can observe a transit when the planetary orbit is aligned with the line of sight. The probability for transit to be observable is

$$\mathcal{P}_{transit} = \frac{R_\star + R_P}{a} \approx \frac{R_\star}{a} \tag{1.8}$$

From the equation, we deduce that the probability that a transit happens depends on the semi-major axis (a) and the stellar radius ($R_\star$). Therefore, the probability decreases

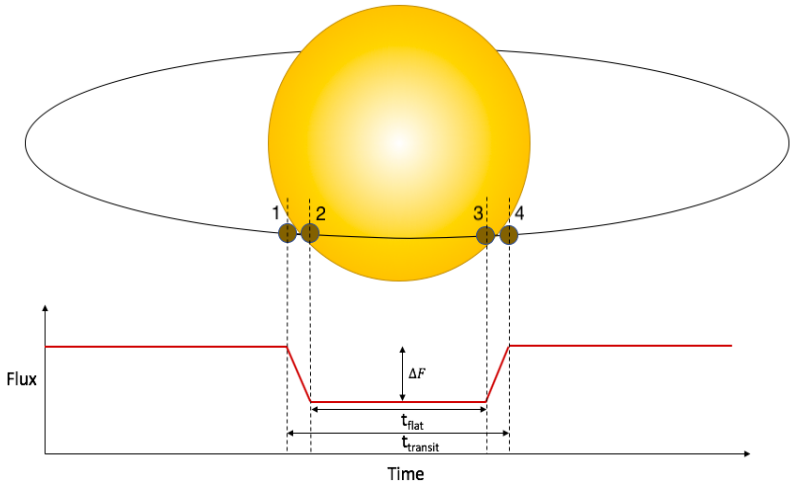

Figure 1.6 Schematized geometry of the transit. Source: Own elaboration.

when the semi-major axis is higher. This analysis is represented in Figure 1.2, when the majority of the exoplanets found with this method have a small semi-major axis in comparison with other methods. In order to catch extrasolar planets is necessary to scan the sky, following a large number of stars for a long period. For this reason, different surveys have been developed. From the ground-based, some project are: HATNet (Bakos et al., 2004), TrES (Alonso et al., 2004), XO (McCullough et al., 2005), SuperWASP (Pollacco et al., 2006), KELT (Pepper et al., 2007), NGTS (Chazelas et al., 2012) and QES (Alsubai et al., 2013). As we mentioned previously, observe from the space, have many advantages. Therefore, have been employed several space mission: e.g. Kepler (Borucki et al., 2010a), CoRoT (Barge et al., 2008), TESS (Ricker et al., 2009), CHEOPS (Broeg et al., 2013) and PLATO (Rauer et al., 2014).

1.1.5 Direct Imaging

In comparison with the other methods described previously, direct imaging is a direct method. This means that we observe the planet directly, in spite of the planets being a faint light source in comparison with the stars. Therefore it is possible to detect planets through the reflected light from the host star (using visible wavelength) or by its thermal

emission (using infrared wavelength). As we can see in Figure 1.2 this method is sensitive to planets with wide orbits ($a > 5AU$), this is due to the difficulty obtaining an image of a planet, which is outshined by its host stars light. For this reason, this technique represents a great challenge. By way of example, if a star like the Sun and Jupiter, the brightest planet in our Solar System, were located at a distance of 10 pc from us, the planet would have only 10^{-9} of the optical flux of the host star, with an angular separation of 0.5 arcseconds. For extrasolar planets are expected to range from 10^{-5} in infrared to 10^{-10} in the optical.

In 2004 the first extrasolar planet found with this method was 2M1207b (Chauvin et al., 2004) with a mass of 4 M_J orbiting at 46 AU around a brown dwarf that was discovered using adaptive optics NIR instrument NACO (NAOS/CONICA, Lenzen et al. 2003) mounted on UT4 telescope of the ESO VLT located in Paranal, Chile. After this discovery, the direct imaging detected 106 planets (see Figure 1.1), for which we show some of the most important discoveries. 51 Eridani b (Macintosh et al., 2015) was discovered using GPI (Gemini Planet Imager, Macintosh et al. 2012), which consists of a high-order adaptive optics system, a coronagraphy, a calibration interferometer, and an integral field spectrograph. GPI was mounted on the Gemini South Telescope at the Las Campanas Observatory in Chile. The importance of this discovery, in addition to being the first exoplanet discovered with GPI, is that this planet is a million times fainter than its host star and was the first extrasolar planet that shows the strongest methane signature, giving additional clues as to how 51 Eridani b formed.

Another important discovery is the detection of the first multiplanet system with this technique using angular difference imaging, which combined many short exposures to reveal faint features (see Figure 1.7). Three giant planets were directly observed orbiting the A5V star HR 8799 (Marois et al., 2008), using telescopes at both the Keck Observatory and Gemini Observatory.

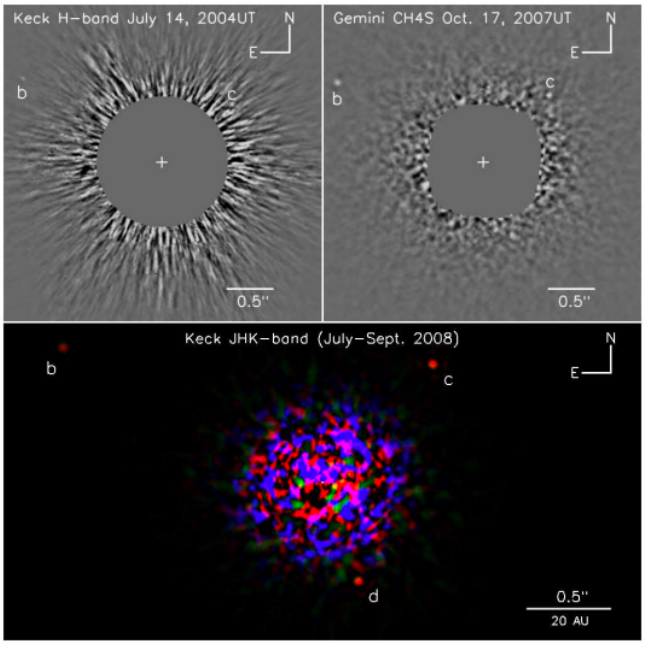

Figure 1.7 Three giant planets around HR 8799 discovered with direct imaging. Source: From Marois et al. (2008).

1.2 The Transit Method

In Section 1.1.4, we explained that when a planet crosses in front of its host star, it is possible to appreciate a drop in the brightness. We can visualize this behavior in the light curve (see Figure 1.6), which is a graph of the flux, as a function of the time. With the help of the light curve, we can derive information about the physical characteristics, that we will describe in Section 1.2.1.

Although the transit method is known as an efficient technique to detect an extrasolar planet, we need to be careful, because the only way to confirm the candidates is through the combination with other techniques, like radial velocity. Therefore, if we only count with photometric data, we need to discard all the possible astrophysical mimics, which will be discussed in Section 1.2.2.

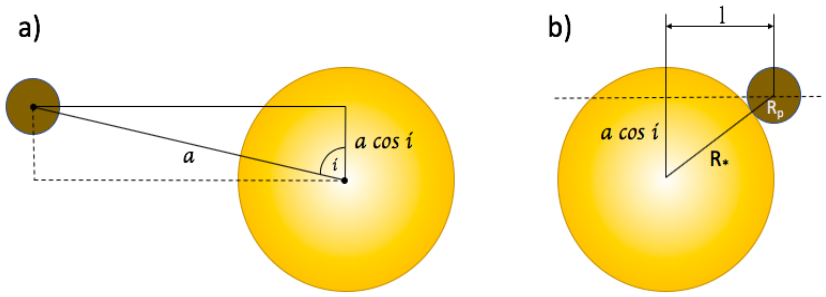

Figure 1.8 The geometry of a transit. (a) Schematic representation of the impact parameter. (b) Schematic representation of the Pythagoras's theorem. Source: Own elaboration

1.2.1 Transit Theory

As we explained previously, through the planetary transit measured in the stellar light curve, we can obtain different physical parameters. First we make the following assumptions (Seager & Mallén-Ornelas, 2003):

1-. The planet is in a circular orbit.

2-. The stellar intensity is uniform across the stellar disk.

3-. The planet is dark compared to the central star.

4-. The light comes from a single star.

In Figure 1.6, we can see that when a planet crosses in front of the star, it blocks some of the starlight during the eclipse. That decrease in the flux called the transit depth depends on the size of the star and the planets, described by the following equation:

$$\Delta F \equiv \frac{F_\star - F_{transit}}{F_\star} = \left(\frac{R_P}{R_\star}\right)^2 \tag{1.9}$$

Where $F_\star$ is the flux measured from the star, $F_{transit}$ is the flux estimated when the planet crosses in front of the star, R_P is the planet radius and $R_\star$ is the stellar radius. With this equation, we can immediately estimate the size of the planet, in terms of the size of its host star.

Through Kepler's third law, we can obtain the semi-major axis of the orbit, described by

$$a = \left(\left(\frac{P}{2\pi}\right)^2 G(M_\star + M_P)\right)^{1/3} \tag{1.10}$$

where P is the orbital period, G is the universal gravitational, $M_\star$ and M_P are the stellar mass and the planetary mass, respectively.

With the period measured from observations and the semi-major axis calculated previously, it is possible to deduce the orbital speed given by

$$v = \frac{2\pi a}{P} \tag{1.11}$$

Also, in Figure 1.6 we can observe that it is possible to determine the time of the transit from the first contact until the four contacts. But if the planet crosses the center of the stellar disc the transit duration is longer than if the planet crosses the star with another inclination. This orbital inclination i is related to the impact parameter b (see a) in Figure 1.8), defined as the projected distance of the center of the planet to the center of the star, given by the following equation:

$$b = \frac{a\cos i}{R_\star} \tag{1.12}$$

We can deduce the path length that the planet takes when crossing the disk of the star (see b) Figure 1.8) from the Pythagoras's theorem, given by:

$$l = \sqrt{(R_\star + R_P)^2 - (bR_\star)^2} \tag{1.13}$$

From the length, l it is possible to derive the transit duration, as illustrated in Figure 1.9. The extrasolar planet moves from A to B around its orbit, creating the angle α in radians. The arc length produced by these points is $a\alpha$, and the distance along a straight line between A and B is $2l$. The distance around an entire orbit is $2\pi a$. From the points

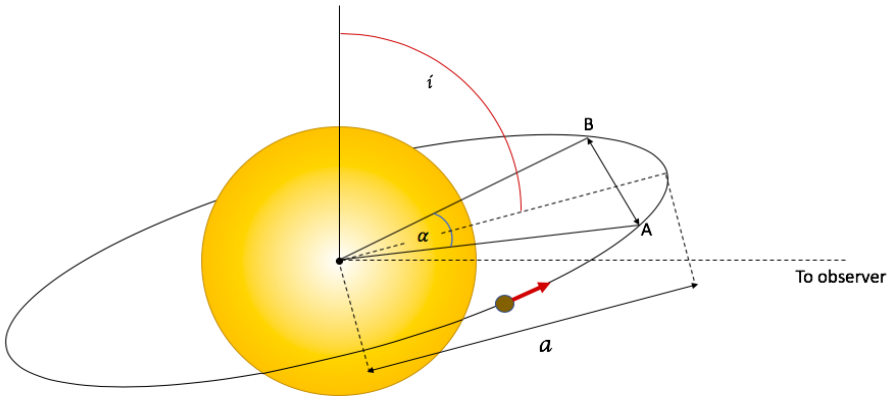

Figure 1.9 Schematized geometry of the orbital of an exoplanet in transit. Source: Own elaboration

A, B and the center of the star we obtain $\sin(\alpha/2) = l/a$, thus:

$$t_{transit} = \frac{P}{\pi} \arcsin\left(\frac{(R_\star - R_P)^2 - (a\cos i)^2}{a^2}\right)^{1/2} \tag{1.14}$$

Finally, we can derive the shape of the transit light curve by calculating the ratio of the duration of the flat part to the total transit duration:

$$\left(\frac{t_{flat}}{t_{transit}}\right)^2 = \frac{\left(1 - \frac{R_P}{R_\star}\right)^2 - \left(\frac{a}{R_\star}\cos i\right)^2}{\left(1 + \frac{R_P}{R_\star}\right)^2 - \left(\frac{a}{R_\star}\cos i\right)^2} \tag{1.15}$$

1.2.2 False Positives

When we observe a light curve, and that shows the typical transit shape, we must take into consideration that it is not always a planet. We can be in the presence of a false positive. A scheme of the different imposters identified that could mimic the transit shape is shown in Figure1.10 listed below are the main false positives:

• Blended eclipsing binary: This false positive happens when a third star dilutes the light of transiting binary system (see a) in Figure1.10). The third star can be part of a hierarchical system associated with each other or can be an isolated star blended with

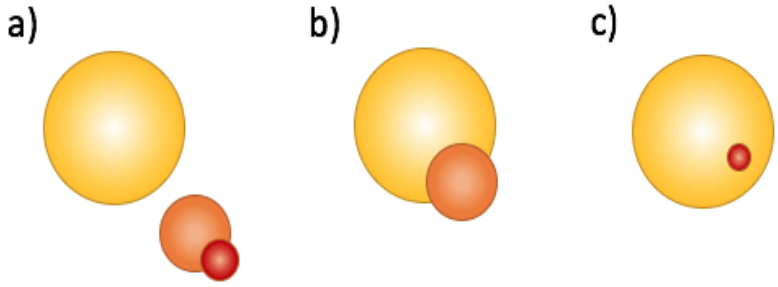

Figure 1.10 Scheme of false positives: a) Blended eclipsing binary. b) Grazing eclipsing binary. c) Planet-sized stars. Source: Own elaboration.

an eclipsing binary, because they are at different distances along the same line of sight. Therefore, the third star dilutes the eclipse depth and produces a shallow dip comparable to a planetary transit.

• Grazing eclipsing binary: We can distinguish easily the depth that the eclipsing binary stars produce because these are deeper in comparison with the dips created by the transit of a planet. As we mentioned before, the depth of the transit is described by the ratio of radii of the host star and the planet. But this equation assumes that the entire disk of the planet is inside the disk of the host star. But when two stars have a misaligned orbit with respect to our line of sight and one star grazes the limb of the other star, the depth is comparable to a planetary sized companion (see b) in Figure1.10).

• Planet-sized stars: If in a binary system the secondary star is smaller than the primary, for example, a white dwarf star or a brown dwarf star. These stars have the same size as gas giant planets (see c) in Figure1.10), but these planets are less massive than the brown dwarf or white dwarf stars. In addition, the transit shape is identical in these three cases to the planetary transit scenario. Therefore with photometric measurements, we can not discriminate between these different possibilities. One way to know the nature of the system is through spectroscopic measurements.

Other possible false positive can be given due to the photometric variability through atmospheric variations, the variability of the star or noise produces for instrumental effects.

1.3 Stellar Formation and Evolution

The stellar formation happens when interstellar gas clouds are massive enough to collapse under their own gravitational pull. The gas is heated, thanks to this collapse that transforms gravitational energy into thermal energy. During this process, approximately half of the gravitational energy liberated is converted into thermal energy and the other energy is emitted by radiation. When the mass collapses, the gravitational binding energy is increased. This process liberates energy within the star. Therefore the system becomes more stable. If the mass of the collapsing body is larger than 0.08 $M_{\odot}$, its gravitational energy is sufficient for the central temperatures to reach the critical value necessary for the fusion of hydrogen and a star is born. When the star is in the process of formation, we called it a protostar. Once the star is born, it is located on the zero-age main sequence (ZAMS). The ZAMS curve in the Hertzsprung-Russell (H-R) diagram represents the position of the stars when the hydrogen fusion triggers in their center. While on the main sequence the hydrogen is progressively fused into helium in the center of the star, the structure of the stars readjust and they slowly move away from the ZAMS. We can observe that the main sequence has a certain width in the H-R diagram, even if the stars have the same mass, this is due to a different age or stellar composition. According to the mass, the stars follow different evolutionary paths in the H-R diagram, as explained below:

• **Low-mass stars**: this kind of stars with masses lower than approximately 0.5 $M_{\odot}$ do not have enough gravitational energy to heat their core to temperatures required for helium fusion. Very low-mass stars are completely convective for a large period of their lifetime because the hydrogen of the surface layers can be brought to the core, a large part of the hydrogen in these stars can be burned during their stay in the main sequence. Therefore the time in which these stars are in the main sequence is longer. Stars with masses, lower than $0.16M_{\odot}$ would fall (after a long time in the future) from the main sequence directly to the white dwarf branch. The white dwarfs are remnant stars where the nuclear energy is no longer produced. Consequently, these objects cool off with the time.

• **Intermediate mass stars (Our Sun)**: These stars begin their lifes on the main sequence

while burning hydrogen in their core. When the hydrogen is fused into helium, the center of the star slowly contracts. This contraction produces an increase of the central temperature, and the hydrogen then burns at a faster rate and can also begin to burn in regions outside the core where before the temperature was too low to maintain the fusion. This process generates an increase in the luminosity of the star. When the amount of hydrogen gradually depletes in the star's core, the hydrogen burns in a growing shell outside the center. The energy produced in this shell-burning phase leads to the outer part of the star to expand, forming a red giant star. Meantime, the core keeps contracting, causing an increase in its temperature, which generates a greater nuclear energy production from helium fusion. The critical temperature for helium fusion is approximately 10^8 K. Due to this production of energy, the temperature increases and does not affect pressure. Therefore the core continues to collapse. This produces an increase in the central temperature and the energy production rate. This has an uncontrolled effect that produces a huge rate of helium fusion, called helium flash. This phase is short-lived, and the star's luminosity is greatly increased. Then comes a phase in which the core and the star stabilize, which is called the horizontal branch. In this phase, the star burns helium in its core and the hydrogen is burning in a shell outside the helium-burning core. After about 10^8 years in the horizontal branch, in the star's core the helium is finished, and now it is composed of carbon. Then, the core of the star contracts while the radius of the star increases, as a consequence, the star climbs the asymptotic-giant branch in the H-R diagram and becomes a supergiant. In the center of the star, a white dwarf composed of carbon is forming, where finally the star enters a phase called a planetary nebula. In this phase the outer layers continue to expand, allowing to observe the central white dwarf. This remnant star does not produce any nuclear energy. Thereafter this star cools of and become a cold inert object called black dwarfs.

• **Massive stars**: When we refer to massive stars, we are talking about stars with a mass greater than 10 $M_\odot$. In the same way than the others stars, they begin their lives on the main sequence while burning hydrogen. In the star's core the hydrogen is exhausted, then the star evolves and starts to burn helium to produce carbon and oxygen. Finished

this phase, the core contracts and successively burns carbon, neon, oxygen, and silicon. During each burning phase, the fusion from the previous phase happens in a shell outside the core. When silicon burning ceases, the core contracts and the central temperatures increases. Contrary to the previous phases of evolution, the iron can no longer produce thermonuclear energy. Therefore, the contraction continues until the temperatures in the core are so large that there exist photons of energy sufficient to destroy iron nuclei by photodisintegration reaction. Finally, the core collapses, causing a supernova and creating a new astronomical object called a neutron star. If the mass of this star is more than approximately 3 $M_{\odot}$, the neutron star becomes a black hole. This upper limit is called Tolman-Oppenheimer-Volkoff.

1.4 Planetary Formation and Evolution

When the first extrasolar planet was discovered, our ideas about the planetary system changed, because since then, we only knew our Solar System, where the rocky planets are close to the host star, and gas giant planets have larger orbital radii. But as we described previously, many of the exoplanetary systems discovered have giant planets with an orbit very close to their host stars. The most accepted theory about the formation of giant planets is the core accretion model (described below), where the planets are formed in a region cool enough of the protoplanetary disk, where the water, methane, and ammonia are condensed into solid ice grains. This region called snowline lies beyond about 4 AU from a solar-mass protostar. In this way, the core of the giant planets form, because they accumulate a massive envelope of gaseous material. As we can see, the giant planets are formed at a considerable distance from their stars, but many of the exoplanets found are very close to their stars. It is believed that the giant planets migrate inward because of gravitational interactions with the remaining protoplanetary disk material. The formation and migration of giant planets happen within the first 1-10 million years after the formation of the host star and the formation of terrestrial planet occurs 10-100 million years

after the star formed. Then, we describe the process of planetary formation:

• **Planetesimal Formation**: The planetesimals are bodies typically of a radius of the order of 10 km. In the study of the planetesimal formation, the aerodynamic forces between solid particles and the gas disk are important, because these forces dominate the evolution of particles in the wide size range that lies between dust and solid rocks. The efficiency with which the particles coagulate in a collision environment is also essential.

• **Terrestrial Planet Formation**: Then when the planetesimals have formed, the mutual gravitational interaction controls their further growth. In the formation of terrestrial planets, the only additional role the gas disk plays, which is to give a modest degree of aerodynamic damping of protoplanetary eccentricity and inclination. Although the physics involved, which is Newtonian gravity, is well-understood and straightforward, to form the Solar System's terrestrial planets is a challenge, because there are necessary about $4x10^9$ planetesimals with a radius of 5km.

• **Giant Planet Formation**: Contrary to the case of terrestrial planet formation for the formation of massive planets two theories have been proposed: the core accretion and the disk instability, that we describe below.

Core accretion theory is supported under the assumption that a core grows through two body collision rapidly enough to be able to overcome a certain critical mass before the dissipation of the gas disk. Thus, the core triggers a hydrodynamic instability producing a rapid gas accretion on to the core. With a typical critical core mass of the order of 10 $M_\oplus$, this can result in a giant gaseous planet that is heavy element enriched. The four phases (see Figure 1.11) for the formation of giant planets are:

1-. Core formation: the core grows through two-body collisions, until obtaining a sufficient mass to retain a significant gaseous atmosphere or envelope.

2-. Hydrostatic growth: There is a release of energy, due to the impact on the core and for the gravitational potential energy liberated when the envelope itself contracts, that must be transported across the envelope for radiative diffusion or convection before it loses the protoplanetary disk gas. The core and the envelope grow until the core exceeds a critical mass.

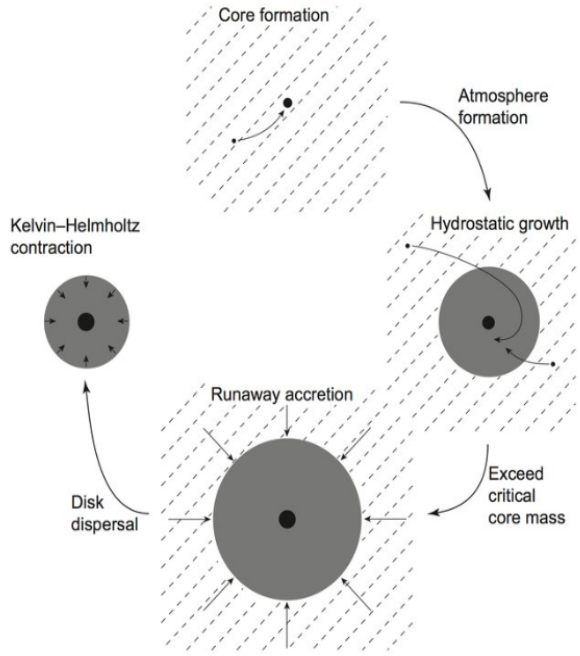

Figure 1.11 Phases of the core accretion theory for the formation of gas giant planets. Source: Armitage (2010).

3-. Runaway accretion: The runaway phase of gas accretion happens when the critical mass is exceeded. In this phase, the supply is limited and defined by the hydrodynamic interaction between the growing planet and the disk.

4-. Termination of accretion: When the amount of gas is exhausted, due to the dissipation of the protoplanetary disk or by the planet opening up a local gap in the disk, the accretion tails finish, and the planets begin a phase of cooling and quasi-hydrostatic contraction.

Disk instability theory rests on the assumptions of the fragmentation into massive planets. It is the result of instabilities that occur in the gaseous protoplanetary disk that was massive enough to be unstable to the instabilities that arise from its own gravity.

1.5 Milky Way Bulge

The Milky Way is a spiral galaxy composed of three parts: the bulge, the disk, and the halo. The bulge is the oldest component of our galaxy. Therefore, it is essential to study different objects in the galactic bulge, to understand the formation and evolution of the Milky Way. We can define the galactic bulge as an over-density that swells up from the plane of the disc. The theories about the formation of the bulge are: the merger-driven bulge scenario that happens during the early stage of the Galaxy, where a bulge is formed violently and quickly by the gravitational collapse or hierarchical merging of sub-clumps of dark matter carry baryons and gas (Abadi et al., 2003; Elmegreen, 1999) and the secular evolution scenario that happens when the bulge structure is born from the dynamical evolution of the stellar Galactic disc (Norman et al., 1996; Athanassoula, 2005). The Milky Way has a box/peanut bulge morphology, which was confirmed directly using the composite IR image from WISE (Ness & Lang, 2016). The bulge shows a metallicity gradients, which has been measured through spectroscopy along the minor axis (Zoccali et al., 2008; Ness & Lang, 2016; Zoccali & Valenti, 2016) and photometrically with a metallicity map covered by the VVV survey (Gonzalez et al., 2013). We have seen some of the observational properties of the galactic bulge, now we focus on the kinematics. The Bulge Radial Velocity Assay survey (BRAVA, Howard et al. 2008; Kunder et al. 2012) presented the mean radial velocity and velocity dispersion with different Bulge latitudes as a function of longitude. As a result that shows a cylindrical rotation of the bulge, which is characteristic of box/peanuts.

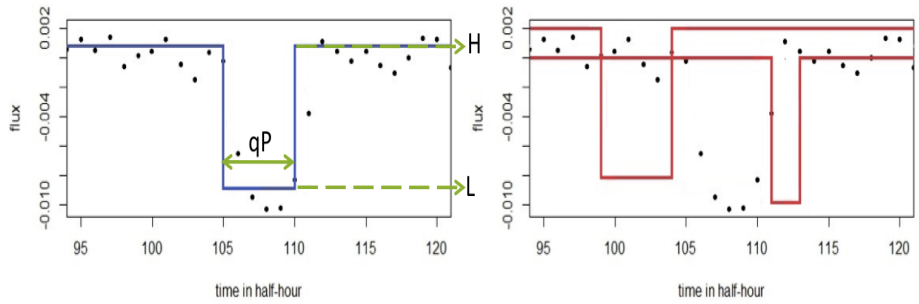

Figure 1.12 Box-shaped functions. Source: Adapted from Zijlstra (2014)[2].

1.6 Periodogram algorithms

Some astrophysical phenomena like stellar variability, eclipsing binaries and transiting planets, can produce periodic time series data. To identify and extract this periodic signal, we used the periodogram. Therefore, a periodogram estimates for different frequencies the significance to identify any intrinsic periodic signals.

In the next sections, we explain three periodogram algorithms: Box-fitting Least Squares, Lomb-Scargle and Phase Dispersion Minimization.

1.6.1 Box-fitting Least Squares

The Box-fitting Least Squares (BLS) algorithm was introduced by Kovács et al. (2002) in order to search in the stellar photometric time series the periodic transits caused by exoplanets. This algorithm has the following assumptions:

1-. The light curve contains a periodic signal with period P

2-. The transit phase only has two discrete values, H and L. This ignores the gradual ingress and egress phases of the transit (see Figure 1.12).

3-. The time spent during the transit phase L as qP, where q is the fractional transit length (small number ~0.01 - 0.05).

4-. The epoch of the transit *e*, which is the position of the transit within a period.

With these assumptions, the BLS algorithm finds the best model from a given set

[2]https://www.math.leidenuniv.nl/scripties/BSC-Zijlstra.pdf

of data points using five parameters: P,q,L,H, and e. The algorithm needs to be fast and efficient, considering that we search for planetary transits in a large number of stars. Therefore BLS ignores the gradual ingress and egress phases of the transit (from the first to the second contact and third to four contacts, shown in Figure 1.6), because the lengths of these phases are short compared to the flat part. According to Kovács et al. (2002) this omission does not affect the results of the search, because we are not interested in the shape properties of the transit. Therefore, now the transit duration ($t_{transit}$) equals to the duration of the flat part of the transit (t_{flat}). Thus, the algorithm uses this box-shaped function to fit the transit data.

Before working with this algorithm we need to center the data set. We can do this subtracting the arithmetic average. This data centering no causes modifications to the structure of the time series. In order to estimate the period P, the BLS algorithm makes use of the technique of data folding, which is using a trial period to fold the time series. Clearly, this parameter is unknown, but we can estimate this parameter based on the previous detections of extrasolar planets to reduce the range from which one chooses the trial period. If the folded time series is very scattered, this is because the trial period has a large deviation with respect to the correct period.

1.6.2 Lomb-Scargle

The Lomb-Scargle (L-S) algorithm (Lomb, 1976; Scargle, 1982) detects and characterizes periodic signals in unevenly-sampled data. This periodogram is optimized to identify in the time series data a sinusoidal-shaped periodic signal. Therefore, this algorithm is not optimal for transiting exoplanets, because the shape of the periodic light curve is not sinusoidal. L-S is a variation of the Discrete Fourier Transform (DFT), where the time series is decomposed into a linear combination of sinusoidal functions. Therefore, the algorithm consists in transforming the data with sinusoidal functions from the time domain to the frequency domain. L-S is composed of a set of formula for the transformation coefficients that is similar to the DFT in the limit of evenly spaced observations. In addition,

an adjustment of the values used to calculate the transform coefficients has been made to make the transform insensitive to time shifts.

However, the Lomb-Scargle does not take into account the measurement errors and a constant term in the fit of the wave function. The solution to these shortcomings is the Generalized Lomb-Scargle periodogram (GLS) developed by Zechmeister & Kürster (2009), which produces more precise frequencies, is less affected to aliasing and provides better determination of the spectral intensity.

1.6.3 Phase Dispersion Minimization

The Phase dispersion minimization (PDM) developed by Stellingwerf (1978) is useful for non-sinusoidal variations for data sets with few observations irregularly spaced.

As in the BLS periodogram, the PDM algorithm folded the time series using a trial period. Once we have the folded data, PDM divides into a series of bins and computes the variance of the amplitude within each bin. If necessary, we can improve the coverage of the phase, overlapping the bins. Then, we combined the bin variance and compared to the overall variance of the data set. We found a true period when the ratio of the bin to the total variances will be small. For a false period, this ratio is close to unity. A plot of these ratios versus the trial periods gives an indicator of the best candidates for periodic components.

1.7 Data

1.7.1 K2 mission

For our study, we used the K2 database, which provides high-precision photometry on the 1 and 30 minute timescales. The Kepler magnitude (K_p) refers to an AB magnitude, ranging from 425 to 900 nm. The Kepler photometer consists of multi CCD modules, and each module covers 5 square degrees on the sky. The observations of K2 consist of a series of observation field “Campaigns” distributed in the plane of the ecliptic.

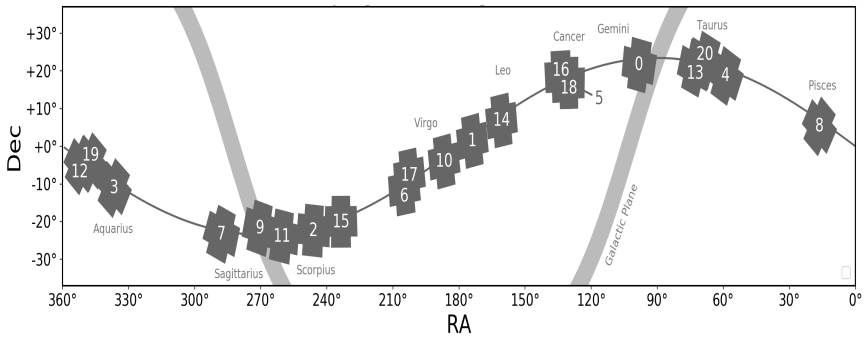

Figure 1.13 K2 campaign fields. Source: The Kepler & K2 website.

Campaign 9 consisting of 19 CCD modules (Figure 2.1, left) covered part of the Galactic Bulge and was dedicated to a microlensing study. In order to increase the data storage, the campaign 9 was split into two parts (campaign 9a and 9b), with a three-day gap from May 19 to May 22, 2016. The campaign 9a is centred at RA=270.3544823 degrees, DEC=-21.7798098 degrees and was observed between April 22 and May 19, 2016. The campaign 9b that was observed between May 22 and July 1, 2016, and is centred at RA=270.3543824 degrees, DEC=-21.7804700 degrees. For our study, we considered only targets from the microlensing super apertures (green area in the Figure 2.1, left), in which 3.3 million pixels were dedicated on five CCD channels.

The campaign 11 consists of 18 CCD modules, due to the loss of CCD module 4. This campaign is centred at RA=260.3880064 degrees, DEC=-23.9759578 degrees (Figure 2.1, right) and covers part of the Galactic Bulge. This campaign was split into two parts with a three-day gap from October 18 to October 21, 2016: the campaign 11a that was observed between September and October 2016 during 23 days and the campaign 11b was observed between October and December 2016 during 48 days.

1.7.2 The VISTA Variables in the Vía Láctea Survey

The VISTA Variables in the Vía Láctea (VVV) survey (Minniti et al., 2010; Saito et al., 2012) that covers a bulge area of 300 square degrees between $-10^\circ < l < +10^\circ$ and

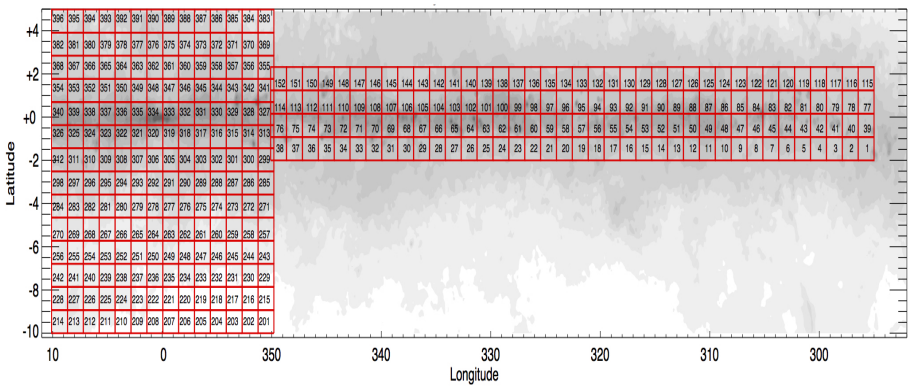

Figure 1.14 VVV survey area. Source: From the VVV survey website.

$-10° < b < +5°$ is divided into 196 tiles.

This survey provides near-infrared photometry in five broad-band filters: Z (0.87 μm), Y (1.02 μm), J (1.25 μm), H (μm) and, K_s (2.14 μm). We used the VVV photometric catalogue that was obtained from the Cambridge Astronomical Survey Unit (CASU) [3] in different tiles in the galactic bulge. The K2-VVV areas of overlap are shown in Figure 2.1.

[3]http://casu.ast.cam.ac.uk/vistasp/

2

Search for Exoplanetary Transits in the Galactic Bulge

The content of this chapter has been accepted in Monthly Notices of the Royal Astronomical Society (arXiv:1811.09174) as "Search for Exoplanetary Transits in the Galactic Bulge" by C.C.Cortés, D. Minniti and S. Villanova.

2.1 Abstract

A search for extrasolar planetary transits using the extended Kepler mission (K2) campaigns 9 and 11 revealed five new candidates towards the Galactic bulge. The stars EPIC 224439122, 224560837, 227560005, 230778501 and 231635524 are found to have low amplitude transits consistent with extrasolar planets, with periods $P = 35.1695, 3.6390, 12.4224, 17.9856$, and 5.8824 days, respectively. The K2 data and existing optical photometry are combined with the multi-band near-IR photometry of the VVV survey and 2MASS in order to measure accurate physical parameters for the host stars. We then measure the radii of the new planet candidates from the K2 transit light curves and also estimate their masses using mass-radius relations, concluding that two of these candidates could be low mass planets, and three could be giant gaseous planets.

2.2 Introduction

The Kepler mission (Borucki et al., 2010b, 2011) was a clear success and a revolution for extrasolar planet studies. The main mission lasted four years and the data collected is still producing extrasolar planets, that are now counted by the thousands. The extended Kepler mission called K2 consisted of several campaigns, with multiple fields observed along the ecliptic plane since 2014. Among a variety of studies, K2 has discovered more than a hundred transiting extrasolar planets up to now (Montet et al., 2015; Schlieder et al., 2016; Van Eylen et al., 2016; Johnson et al., 2016; Adams et al., 2016; Sinukoff et al., 2016; Barros et al., 2016; Pope et al., 2016; Dressing et al., 2017a,b; Petigura et al., 2018; Wittenmyer et al., 2018; Mayo et al., 2018; Yu et al., 2018; Crossfield et al., 2018; Livingston et al., 2018).

We are interested here in the data from campaigns 9 and 11 (hereafter K2C9 and K2C11), that observed the Milky Way bulge. This is a crowded and reddened region of our Galaxy, but of great interest, because it overlaps with our ongoing VVV survey, that has been mapping the whole bulge in the near-IR since 2010 (Minniti et al., 2010; Saito et al., 2012). The challenge is the large Kepler 4 arcsec pixel scale, as discussed extensively elsewhere by Henderson et al. (2016) and Zhu et al. (2017). We use our higher resolution VVV images (with 0.3”/pixel scale) in order to weed out bad candidates (usually blended objects). In particular, Henderson et al. (2016) describe in detail the goals, difficulties, and procedures of the K2C9.

We started a project to detect and study new transiting exoplanets in the Galactic Bulge, using K2 mission and VVV survey data. We report here the discovery and characterization of five exoplanetary candidates in the bulge. This is organized as follows, in Section 2.3 discusses our search. In Section 2.4.1 and 2.4.2 we give the physical parameters for the sample stars and planets, respectively. The discoveries are discussed in turn in Section 2.5.

2.3 Light Curves Analysis

For the exoplanet candidates search, we used 875 light curves from the campaign 9 and 13.607 light curves from the campaign 11, that were extracted by Vanderburg & Johnson (2014). Both campaigns were split into two parts, therefore we normalized the flux of the light curve for part a and b (see section 1.7.1) using a cubic spline function. We choose the order of the polynomials according to the light curve. After the fitting, we removed upwards outliers, which are caused by cosmic rays or asteroids and also, we removed the downward outliers making sure that the transit was not removed. After flattening the light curves, we calculated a Box Least Squares (BLS)[1] periodogram Kovács et al. (2002), to detect a periodic signal. We used the definition of Vanderburg et al. (2016) to perform the period search ranging from 2.4 hours to half the length of the campaign and the spacing between periods expressed as:

$$\Delta P = P\frac{D}{N \times T_{tot}}$$

where ΔP is the spacing between periods, P is the period tested, D is the transit duration at that period, N is an oversampling factor and T_{tot} is the total duration of the campaign.

After this process, we cleaned our catalogue by applying some restrictions. From the analysis described by Vanderburg et al. (2016), we considered targets that in the BLS periodogram have at least one peak with $S/N > 9$. Also, we eliminate objects whose duration is greater than 20% of the detected period, and we considered only detections that have two or more transit events.

Even when an object passes these tests, there is the possibility that it is a false positive. For this reason, we performed a visual inspection to discard obvious false positives such as spurious detections, eclipsing binaries and any other astrophysical false positives.

Additionally, we take advantage of the near-infrared data from the VVV survey that overlapped with the K2 data (see Figure 2.1), to discard false positives, specially blended objects, because with this photometry we can constrain the contaminant stars with a different colour than the target.

[1] https://github.com/dfm/python-bls

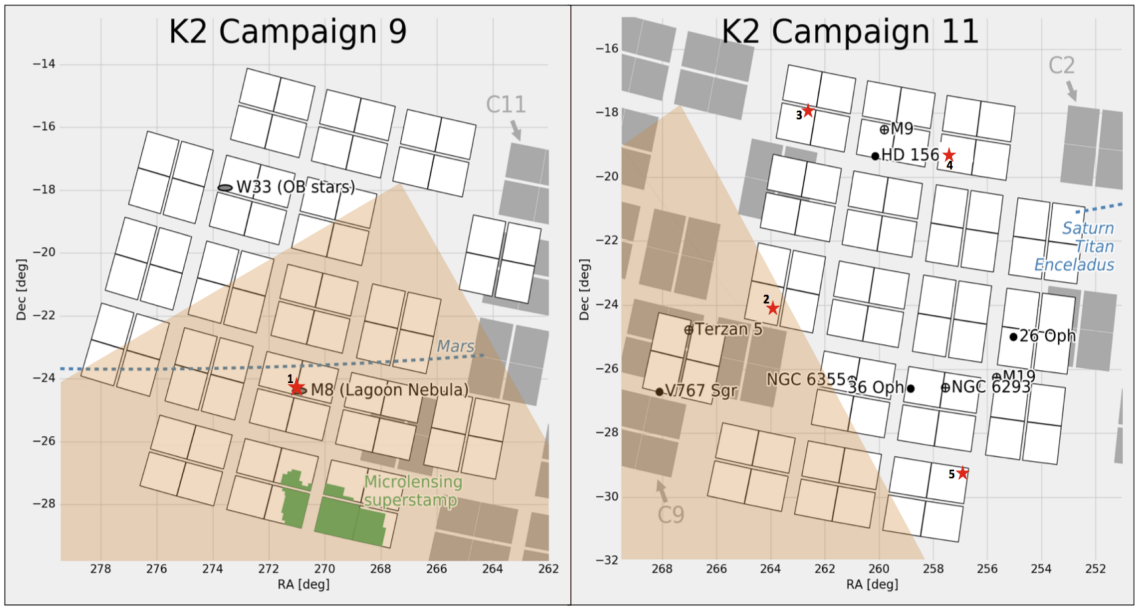

Figure 2.1 The figure shows the two K2 campaign fields: campaign 9 (left) and campaign 11 (right), in which we perform the search for extrasolar planets. The red stars represent the position of the exoplanet candidates that we found in our study with their respective numbers (see table 2.3). The green area in campaign 9 represents the microlensing super apertures. The overlapped coloured region corresponds to the region mapped by the VVV survey. This plot is taken from the Kepler & K2 website.

Our final catalogue contains five planet candidates (see table 2.3). The planetary parameters estimation is explained in section 2.4.2.

2.4 Physical Properties

2.4.1 Stellar Properties

The stellar parameters of the host stars of our exoplanet candidates are summarized in Table 2.1. Based on previous studies, the host star 224439122 was catalogued as a variable Weak T tau (Prisinzano et al., 2012) with a period 5.8775 days (Henderson & Stassun, 2012).

The stellar parameters for our exoplanet candidates were estimated through Gaia DR2

(Andrae et al., 2018), whose information was extracted from Gaia Archive[2] (Gaia Collaboration et al., 2016, 2018). The radius of the host star 231635524 cannot be derived from data in Gaia DR2, because stars with fractional parallax uncertainties greater than 20 percent are not reliably inverted to yield distances. This particularly affects distant and/or faint stars (Andrae et al., 2018). For the host star 231635524, the fractional parallax uncertainty is 450 percent (Bailer-Jones et al. 2018 infer a distance in excess of 10 kpc with large errors). It is most likely this host star is at least a giant, since this star is too bright to be a dwarf, given the likely very long distance.

We classify our host stars by calculating the reduced proper motion, after properly correcting for extinction. For the passbands in the VVV survey, we measured the extinction using the reddening maps of Gonzalez et al. (2012) by the tool BEAM (Bulge Extinction And Metallicity) calculator[3] using the Cardelli et al. (1989) extinction law. In the case of filters in the 2MASS catalogue, we used Schlegel et al. (1998) maps through the tool Galactic DUST Reddening & Extinction[4]. The photometric parameters are summarized in Table 2.2.

With the proper motion of Gaia DR2 catalogue, we calculated the reduced proper motion of our host stars, through the equation defined as:

$$H_J = J + 5\log\mu \tag{2.1}$$

where J is the J-band magnitude and μ is the total proper motion. With the criteria defined by Rojas-Ayala et al. (2014):

$$H_J^{dwarf} > H_J^* = 68.5(J - K_s) - 50.7 \tag{2.2}$$

we classify the host star like dwarf or giant, where H_J^* is the dwarf/giant discriminator.

[2]https://gea.esac.esa.int/archive/
[3]http://mill.astro.puc.cl/BEAM/calculator.php
[4]https://irsa.ipac.caltech.edu/applications/DUST/

2.4.2 Planetary Parameters

We have found five planet candidates, with the period and depth calculated from the output of the BLS algorithm. Assuming that the orbit is circular, we modeled the transit time, the period, the planetary to stellar radius ratio ($R_p/R_\star$), the semi-major axis normalized to the stellar radius ($a/R_\star$) and the inclination, through a transit model using the BAsic Transit Model cAlculatioN (BATMAN) [5] Python package (Kreidberg, 2015). For the development of our model, we used the quadratic limb darkening law (Kopal, 1950) with the coefficient estimated by Kreidberg (2015).

In order to take into account the smearing effect of the 30 min cadence of the K2 data (Kipping, 2010), we used the supersampling provided by BATMAN, that consists in calculating the average value of the light curve from the evenly spaced samples during an exposure.

After that, we measured the transit parameters and their uncertainties of this model using emcee[6] Python package (Foreman-Mackey et al., 2013), which is an implementation of the affine-invariant ensemble sampler for Markov Chain Monte Carlo (MCMC) (Goodman & Weare, 2010). We implement the same uncertainties to each flux, because the flux error was not calculated in the K2 data reduction process.

We estimated the mass of the planet candidates through Forecaster[7] Python package developed by Chen & Kipping (2017), which uses a probabilistic mass-radius relationship. With this code it is possible to predict the mass of the candidates based on a given radius measured previously.

The estimation of the planetary parameters is summarized in Table 2.3. The exoplanet candidates with the fitting model are shown in Figure 2.2 to Figure 2.6.

[5] http://astro.uchicago.edu/ kreidberg/batman/tutorial.html
[6] http://dfm.io/emcee/current/
[7] https://github.com/chenjj2/forecaster

2.5 Discussion and Conclusions

In this work, we present the discovery of five exoplanet candidates, which were detected with the transit method using K2 photometry. One of the parameters that we can obtain with this method is the planetary radius. To determine this parameter, we need the stellar radius, which was calculated photometrically (see Section 2.4.1). To definitely classify these candidates is it is necessary to estimate their masses, which are not possible to measure using this technique. Clearly, spectroscopic observations are needed for these candidates. Therefore, we predict the mass through the code Forecaster (see Section 2.4.2), which uses a mass-radius relationship. Even though these parameters are not highly accurate, they represent a good initial estimate to perform our analysis and give a preliminary idea about the nature of our candidates.

We compared our candidates with the mass-density relationship proposed by Hatzes & Rauer (2015). The relationship is based on the inflections in the mass-density diagram, and shows three regions. The regions are low mass planets, giant gaseous planets and stellar objects. Then, we proceed to analyze each of our candidates:

EPIC 224439122b is a candidate exoplanet orbiting the host star located in NGC 6530 (open cluster), classified as a variable Weak T Tau star with spectral type M0-M1 V (Prisinzano et al., 2012) with a period 5.8775 days (Henderson & Stassun, 2012). This extrasolar planet candidate has two transits and has a period 35.1695 days, indicating that it could be a warm Jupiter (the orbital period between 10 and 100 days). Also, this is the largest candidate in our sample with R=48.1$R_\oplus$ and an estimated mass of M=438.0M_J, implying that it could be a stellar object ($M > 60M_J$, Hatzes & Rauer 2015). As the largest planets known have radii of $\sim 20R_\oplus$, this radius seems to be too large for an exoplanet. Although this candidate has a depth of $\sim 5\%$ and a large mass, we consider that this object passed the test described in Section 2.3 to discard false positive. Also, as we mentioned above, we do not measure the mass and the stellar parameters. Therefore these are not entirely reliable.

EPIC 224560837b is a candidate with nineteen transit events with a period of 3.6390 days, which is within the definition of hot Jupiters (the orbital period between 1 and 10 days). This candidate has a radius of $30.6R_{\oplus}$ and an estimated mass of $260.8M_J$ indicating that it could be a stellar object ($M > 60M_J$, Hatzes & Rauer 2015). Despite this candidate is the second largest in our sample and according to the mass classification this could be a stellar object, we take into account that this target passed the test mentioned in Section 2.3 and the estimation of the stellar parameters and the planetary mass were not measured. For this reason, we do not discard the possibility that this object could be an extrasolar planet.

EPIC 227560005b has a period of 12.4224 days. This candidate has four transits and is our smallest exoplanet candidate with a R=$2.0R_{\oplus}$ and an estimated mass of $0.02M_J$ indicating that it could be a low mass planet ($M < 0.3M_J$, Hatzes & Rauer 2015). The same definition would apply for **EPIC 230778501b** that has three transits with a period of 17.9856 days. This candidate is the second smallest in our sample with R=$2.2R_{\oplus}$ and an estimated mass of $0.02M_J$.

EPIC 231635524b is a candidate that has eleven transits with a period of 5.8824 days. According to the period, this could be a hot Jupiter. As we explained in Section 2.4.1, the radius of the host star 231635524 is not available in Gaia DR2, and we infer that this star could be a giant. Therefore if 231635524 could be a giant and the planetary to stellar radius ratio is 0.132 (see Table 2.3) probably our candidate could be a giant gaseous planet.

Finally, we reported the discovery of five exoplanet candidates detected in the Galactic Bulge with K2 data with orbital periods between 3.6390 and 35.1695 days and planetary radii in the range of 2.0 to 48.1 $R_{\oplus}$. These planet candidates orbit host stars with a range of magnitudes and temperatures ($12.039 < K_p < 16.072$, and 4184 K $< T_{eff} <$4647 K).

Additionally, two of our candidates were classified as stellar objects (224439122 and 224560837) and two as low mass planets (227560005 and 230778501) according to Hatzes & Rauer (2015), but we considered that 224439122 and 224560837 passed the test to discard false positive mentioned in Section 2.3, therefore there are the possibility

that these targets could be planets. Due to the radius for the host star of the candidate 231635524 is not available in Gaia DR2, we can not estimate the planetary radius, and consequently, we can not predict the mass of the planet. Therefore, as we explained in Section 2.5, we infer that the candidate 231635524 could be a giant gaseous planet.

In addition, we emphasize that the stellar parameters were determined using photometry, and that the derived masses in particular are very uncertain. Therefore, we would like to encourage follow-up spectroscopic observations in order to confirm our exoplanet candidates and to refine their physical parameters.

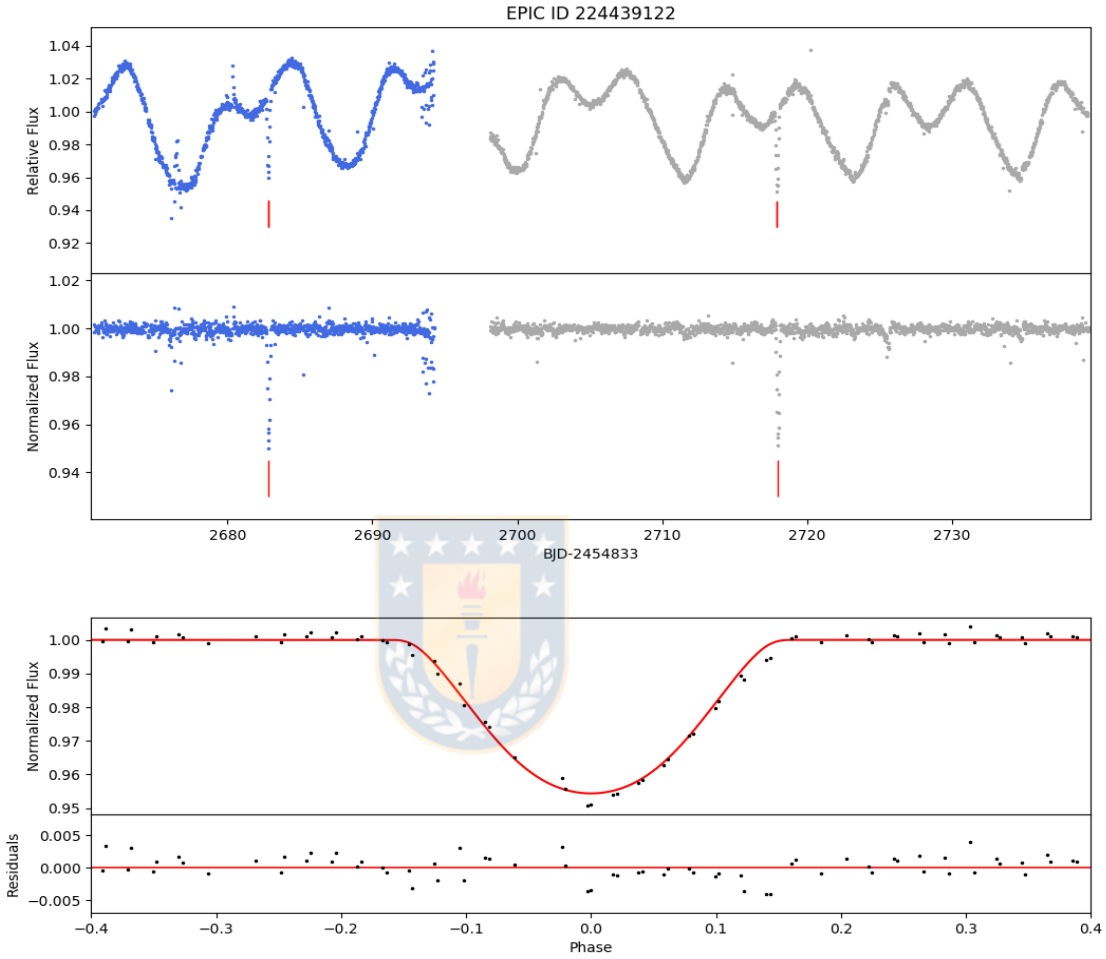

Figure 2.2 Light curve of the exoplanet candidate 224439122. Top: Light curve from the campaign 9 of the exoplanet candidate 224439122 orbiting a variable star. As we mention in the section 1.7.1 the campaign was split into two parts: the blue points indicate c9a and the gray points indicate c9b. The red lines show two transit times. Middle: Flattened light curve of EPIC ID 224439122 (see section 2.3). Bottom: Phase folding of the normalized light curve and residuals. The black points mark the K2 data, and the red line marks the best-fitting transit model. This candidate could be a gaseous giant with a period of 35.1695 days.

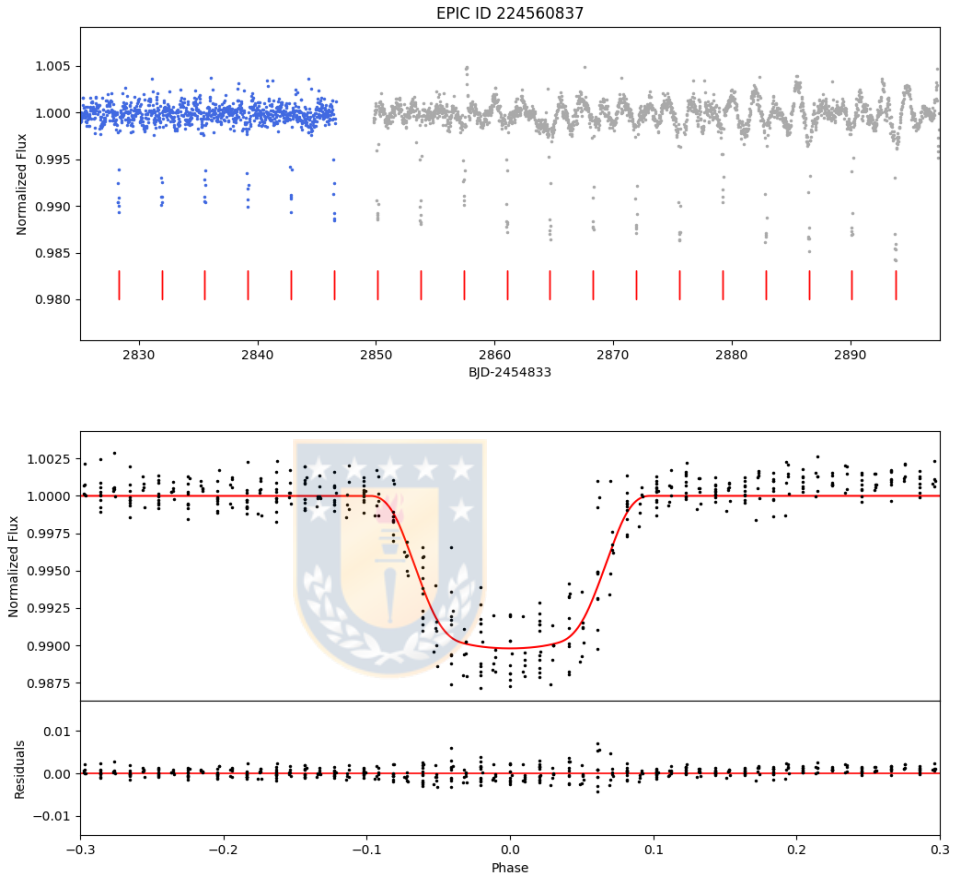

Figure 2.3 Light curve of the exoplanet candidate 224560837. Top: Flattened light curve from the campaign 11 of the exoplanet candidate 224560837. The blue points indicate c11a and the gray points indicate c11b. The red lines show nineteen transit times. Bottom: Phase folding of the normalized light curve and residuals. The black points mark the K2 data, and the red line marks the best-fitting transit model. This is a possible gaseous giant in a 3.6390 days orbit.

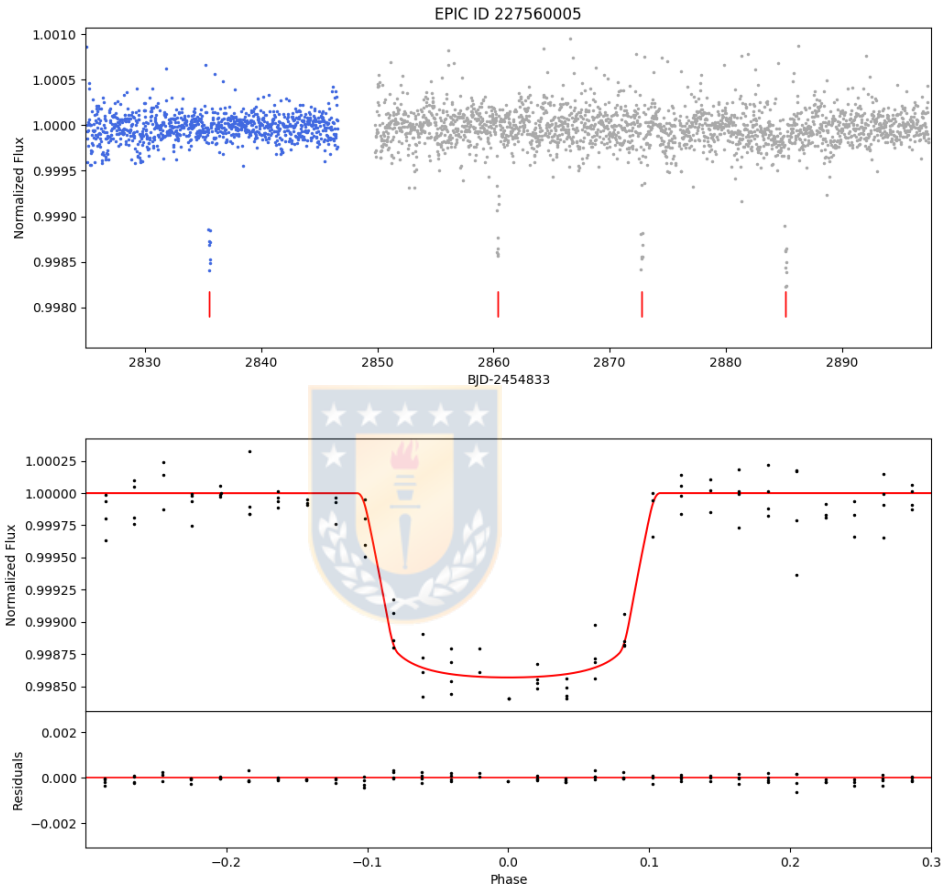

Figure 2.4 Light curve of the exoplanet candidate 227560005 from the campaign 11. See Figure 2.3 caption. This target could be a low mass planet with period P=12.4224 days and four transit events.

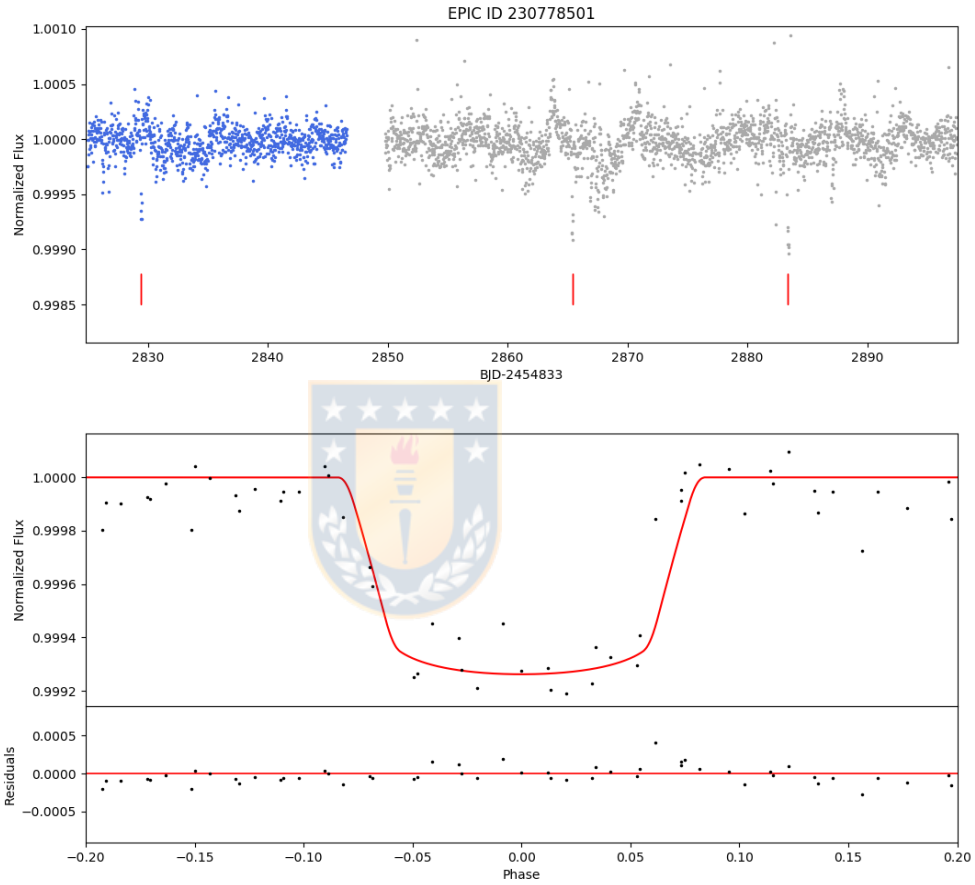

Figure 2.5 Light curve of the exoplanet candidate 230778501 from the campaign 11. See Figure 2.3 caption. This target could be a low mass planet with a period of 17.9856 days and three transit events.

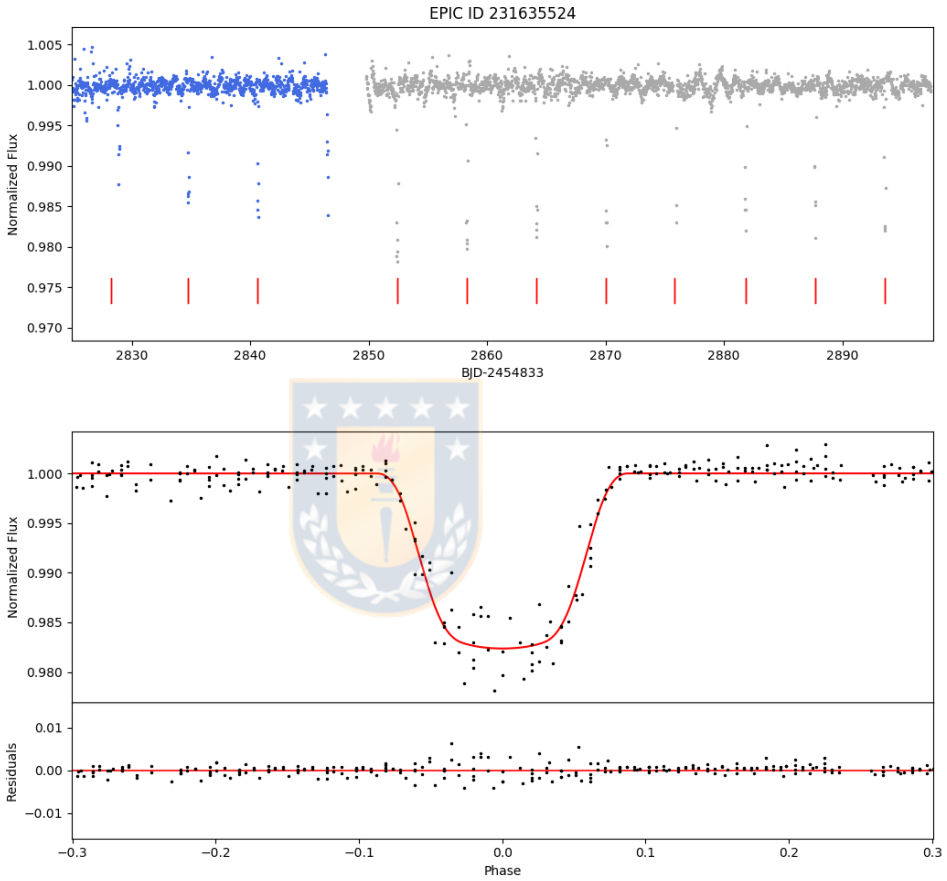

Figure 2.6 Light curve of the exoplanet candidate 231635524 from the campaign 11. See Figure 2.3 caption. This target could be a gaseous giant with a period P=5.8824 days and eleven transit events.

Table 2.1 Stellar parameters

ID	EPIC ID	RA (J2000, h:m:s)	DEC (J2000, d:m:s)	T_{eff} (K)	$R_\star$ ($R_\odot$)	RPM H_J	classification
Campaign 9							
1	224439122	18:04:44.11	-24:14:39.06	$4348^{+106(1)}_{-190}$	$1.96^{+0.18(1)}_{-0.09}$	$-2.60^{(1)}$	Dwarf
Campaign 11							
2	224560837	17:35:13.92	-24:01:42.35	$4191^{+217(1)}_{-199}$	$2.75^{+0.28(1)}_{-0.26}$	$-1.09^{(1)}$	Dwarf
3	227560005	17:31:02.07	-17:50:35.39	$4184^{+124(1)}_{-179}$	$0.51^{+0.05(1)}_{-0.03}$	$4.20^{(1)}$	Dwarf
4	230778501	17:09:39.53	-19:13:01.41	$4647^{+141(1)}_{-134}$	$0.73^{+0.04(1)}_{-0.04}$	$3.24^{(1)}$	Dwarf
5	231635524	17:07:33.40	-29:16:21.27	$4322^{+277(1)}_{-75}$	-	$1.80^{(1)}$	Giant

Note. RPM H_J is the reduced proper motion of the star. RPM H_J was calculated using the equation (1), with the proper motion from Gaia DR2 catalogue. In column 10, we classify the host star as giant and dwarf according to the criteria defined by Rojas-Ayala et al. (2014) equation (2).
References. (1) Gaia Collaboration et al. (2016, 2018).

Table 2.2 Photometric parameters

ID	EPIC ID	K_p (mag)	U (mag)	B (mag)	V (mag)	R (mag)	I (mag)	z (mag)	Y (mag)	J (mag)	H (mag)	K_s (mag)
Campaign 9												
1	224439122	16.072	17.445[1]	17.445[1]	16.145[1]	-	14.560[1]	14.132[2]	13.786[2]	10.395 [2]	10.878[2]	11.257 [2]
Campaign 11												
2	224560837	14.931	-	16.443[3]	15.174[3]	14.723[3]	-	13.068[2]	12.828[2]	11.525[2]	11.514[2]	11.481[2]
3	227560005	12.039	-	14.132[4]	12.706[4]	12.088[4]	11.402[4]	-	-	9.517[5]	9.006[5]	8.883[5]
4	230778501	12.388	-	13.794[3]	12.685[3]	12.264[3]	12.007[3]	-	-	10.351[5]	9.879[5]	9.760[5]
5	231635524	14.749	-	14.940[6]	14.030[6]	-	-	-	-	12.311[5]	11.787[5]	11.709[5]

Note. K_p is the Kepler magnitude described in the section 1.7.1. The filter J, H, and K_s were corrected for extinction, as explained in section 2.4.1.

References. (1) Sung et al. (2000); (2) VVV survey (Minniti et al., 2017a); (3) Zacharias et al. (2012); (4) APASS catalogue (Henden et al., 2016); (5) 2MASS All-Sky Survey (Cutri et al., 2003); (6) Zacharias et al. (2005).

Table 2.3 Planetary parameters

ID	EPIC ID	Period (days)	Transit epoch T_0 BJD - 2454833	a/$R_\star$	i (deg)	δ (%)	$R_P/R_\star$	R_P ($R_\oplus$)	M_P ($M_\oplus$)
Campaign 9									
1	224439122	35.1695	2682.8129	$34.09^{+0.16}_{-0.07}$	$88.62^{+0.05}_{-0.02}$	5.05	$0.225^{+0.004}_{-0.009}$	$48.1^{+5.4}_{-0.5}$	$139220.7^{+18450.3}_{-18814.8}$
Campaign 11									
2	224560837	3.6390	2828.2806	$4.95^{+0.19}_{-0.21}$	$80.48^{+0.54}_{-0.62}$	1.04	$0.102^{+0.001}_{-0.001}$	$30.6^{+3.5}_{-3.2}$	$82890.3^{+14961.3}_{-14115.1}$
3	227560005	12.4224	2835.5338	$19.09^{+1.42}_{-1.23}$	$88.68^{+0.30}_{-0.38}$	0.13	$0.036^{+0.002}_{-0.003}$	$2.0^{+0.3}_{-0.3}$	$4.9^{+3.9}_{-2.1}$
4	230778501	17.9856	2829.4447	$27.78^{+1.37}_{-1.77}$	$88.49^{+0.95}_{-0.67}$	0.07	$0.027^{+0.011}_{-0.005}$	$2.2^{+1.1}_{-0.5}$	$6.1^{+4.7}_{-3.3}$
5	231635524	5.8824	2828.8985	$10.17^{+0.50}_{-0.35}$	$85.71^{+0.35}_{-0.26}$	1.76	$0.132^{+0.001}_{-0.001}$	-	-

Note. The Sun and Earth units were obtained from the International Astronomical Union(Prša et al., 2016). The planetary parameters were estimated in the section 2.4.2. T_0 is the time of transit, $a/R_\star$ is the semi-major axis normalized to the stellar radius, i is the inclination, δ is the transit depth, $R_P/R_\star$ the planetary to stellar radius ratio, R_P is the planetary radius, calculated by multiplying the $R_P/R_\star$ values with the stellar radius and M_P is the planet mass estimated using mass-radius relationship developed by Chen & Kipping (2017) through Forecaster Python package.

3

Variability in Red Giant Branch Stars in the Galactic Globular Clusters with VVV survey

The content of this chapter has been published in Astronomy & Astrophysics (2018, vol. 620, N° A96) as "Chemical analysis of NGC 6528: one of the most metal-rich bulge globular clusters" by C. Muñoz, D. Geisler, S. Villanova, I. Saviane, C.C. Cortés, B. Dias, R.E. Cohen, F. Mauro and C. Moni Bidin. Also, the content has been sent for publication in Monthly Notices of the Royal Astronomical Society to be published as: "Chemical Analysis of the bulge Globular Cluster NGC 6553" by C. Muñoz, S. Villanova, D. Geisler, C.C. Cortés, C. Moni Bidin, I. Saviane, R.E. Cohen F. Mauro.

3.1 Abstract

Thanks to the multi-epoch observations in K_s band of VVV survey, we can construct a light curve and search for variability in three Bulge Globular Cluster: NGC 6528, NGC 6553 and NGC 6569. We detected in each of these clusters, one candidate variable star with a period of 0.25729, 29.04823 and 1.45517 days, respectively. These clusters were

part of the study of Muñoz et al. (2018) and Muñoz et al. (2019, in preparation), whose aim was to analyze the behavior of these clusters associated with the Multiple Populations phenomenon. For this reason, he obtained chemical abundance of Red Giant Branch (RGB) stars using high-resolution spectroscopy from FLAMES-UVES. The iron abundance of the stars used to study these clusters are in good agreement with previous studies, except for the candidate variable star of NGC 6528, it is the most metal-poor of the sample.

3.2 Introduction

The globular clusters are the oldest structures in our Galaxy, and the bulge is the oldest galactic component (Cescutti et al., 2018). Therefore, it is essential to study these objects in the galactic bulge to understand the formation and evolution of the Milky Way. The globular clusters contain several kinds of variable stars (Contreras Peña et al., 2018; Martinazzi et al., 2017; Tsapras et al., 2017; Figuera Jaimes et al., 2016; Safonova et al., 2016), which are particularly convenient to study and interpret, due to all the stars in the cluster have the same distance, reddening, composition, and age. But we need to consider some problems when we study the bulge, for instance, the high extinction, the differential reddening, and high crowding (Gonzalez et al., 2012; Nishiyama et al., 2006). The Vista Variables in the Vía Láctea (VVV) survey is perfect to solve these problems because covers most of the bulge region of our Galaxy with near-infrared photometry and multi-epoch in the K_s band (Minniti et al., 2010; Saito et al., 2012).

Previous research has been dedicated to studying the variability in the galactic bulge with the VVV survey (Contreras Peña et al., 2018; Montenegro et al., 2018; Navarro Molina et al., 2016; Alonso-García et al., 2015; Gran et al., 2015). Allowing the detection of new globular clusters, thanks to the discovery of RR Lyrae stars (Minniti et al., 2017b, 2018; Contreras Ramos et al., 2018).

Muñoz et al. (2017, 2018), and Muñoz et al., 2019 (in preparation) performed detailed chemical analysis of bulge globular cluster NGC 6440, NGC 6528, NGC 6553 and NGC

6569 using high-resolution spectroscopic. Muñoz et al. (2018) found a star of the sample is most metal-poor. We thought that probably this discrepancy is the variability. Therefore, we search for variable stars in the last three globular clusters using the multi-epoch of the VVV survey, and we found that this star metal-poor could be a variable star. Also, we detected in each of the globular clusters NGC 6553 and NGC 6569, one candidate variable star.

3.3 Light Curves Analysis

We checked the variability of 21 stars in the bulge globular clusters NGC 6528, NGC 6553 and NGC 6569 using the VVV survey data (Minniti et al., 2010; Saito et al., 2012), which gives us multicolor photometry in five bands: Z (0.87 um), Y(1.02 um), J (1.25 um), H (1.64 um) and Ks (2.14 um). The survey covers a bulge area of 300 square degrees divided into 196 tiles. NGC 6528 is located on tile b278 whose central coordinates are RA: 18:04:40.94 DEC: -30:13:18.5 (J2000). On tile b295, centered at RA: 18:09:54.41 DEC: -25:52:38.3(J2000) is located the globular cluster NGC 6553 and NGC 6569 is located on tile b250 that is centred at RA: 18:13:41.62 DEC:-31:13:58.4(J2000).

For the candidate variable stars search, we used the VVV catalog of aperture photometry for each epoch was obtained from the Cambridge Astronomical Survey Unit (CASU)[1]. The catalog has positions, fluxes, and flags which indicate the most probable morphological classification. In this last case, the flag ”-1”, which was chosen for this analysis, denotes the best-quality photometry of stellar objects, other flags in the catalog are ”0” (noise), ”- 2” (borderline stellar), ”-7” (sources containing bad pixels), and ”-9” (saturated source).

To avoid the dispersion induced for the fluxes measured successively, we performed the average for epochs with a few minutes of separation. After this process, we computed the Generalized Lomb Scargle (GLS) (Zechmeister & Kürster, 2009) and Phase Dispersion Minimization (PDM) (Stellingwerf, 1978) algorithms of each star using aper-

[1]http://apm49.ast.cam.ac.uk/

ture photometry, to detect any periodic signals. We only considered periodic signals with 0.1 % significance by both methods. We estimated the total amplitudes of the light curves through the Fourier fits.

For the candidate variable star of the globular cluster NGC 6528, we verified the variability in this star using point spread function (PSF) photometry. The estimation of the properties of the variable candidates is summarized in Table 3.1.

3.4 Stellar Properties

The photometric parameters of the stars that we found variability are summarized in Table 3.2. The J, H, K_s magnitudes were estimated using VVV PSF photometry (de-reddened) calibrated on the system of 2MASS (Mauro et al., 2014; Cohen et al., 2017). The Z and Y magnitudes are aperture photometry from VVV survey and were extracted by Minniti et al. (2017a).

Muñoz et al. (2018) and Muñoz et al. (2019, in preparation) determined the stellar parameters for the globular clusters NGC 6528, NGC 6553 and NGC 6569 directly from the spectra to avoid the reddening effect.

These data were observed with the fiber-fed multi-object FLAMES facility mounted at the ESO VLT/UT2 telescope in Cerro Paranal (Chile). The FLAMES observations were conducted using the blue and red arms of the high-resolution spectrograph UVES and allowed for the simultaneous observation of seven stars. FLAMES-UVES data have a spectral resolution of about R 47 000. The data was taken with central wavelength 580 nm, which covers the wavelength range 476 - 684nm. Data reduction was performed using the ESO CPL based FLAMES/UVES Pipeline version 5.3.0[2] for extracting the individual fibre spectra. Data reduction includes bias subtraction, flat-field correction, wavelength calibration, and spectral rectification.

Muñoz et al. (2018) and Muñoz et al. (2019, in preparation) selected seven targets for each globular clusters to be observed with FLAMES- UVES from the membership list

[2]http://www.eso.org/sci/software/pipelines/

published by Saviane et al. (2012) using FORS2. The stars used in the study are members of the globular cluster using two criteria: the range of radial velocities of member stars was small and the dispersion in the equivalent widths was comparable to the measurement errors (assuming the intrinsic abundance dispersion in the cluster is small).

These stars belong to the upper RGB, as can be clearly seen in the color-magnitude (CMD) diagram Figure 3.2, Figure 3.4 and Figure 3.6 for the clusters NGC 6528, NGC 6553 and NGC 6569, respectively. The candidate variable star is represented in the color-magnitude diagrams as a red, blue and orange star for the clusters NGC 6528, NGC 6553 and NGC 6569, respectively.

We summarized in Table 3.3 the stellar parameters estimated by Muñoz et al. (2018) and Muñoz et al. (2019, in preparation): the heliocentric radial velocity, the effective temperature, the metallicity and the micro-turbulent velocity.

3.5 Discussion and Conclusions

As we explained in Section 3.3, we computed the Generalized Lomb Scargle and Phase Dispersion Minimization algorithms of each star using aperture photometry, to detect any periodic signals. We found in each of the globular clusters one candidate variable star. See the position of these stars as a red, blue and orange star in the color-magnitude diagrams (Figure 3.2, Figure 3.4 and Figure 3.6) for the clusters NGC 6528, NGC 6553 and NGC 6569, respectively. Below, we proceed to analyze each of the candidates:

Candidate Variable Star in NGC 6528: We detected a significant variability in star #5 (see Figure 3.2) of the seven stars that Muñoz et al. (2018) analyzed in his study. After this previous confirmation, we verified the variability in this star using point spread function (PSF) photometry. We obtained a total of 73 epochs (see Figure 3.1, top left) in the K_s band from April 2010 to September 2015, in a range of 10.631 < K_s <10.704 mag with error of 0.02. We found a period of 0.25729 days, as shown in Figure 3.1 (top right) we detected a strong peak on the Generalized Lomb-Scargle periodogram. When

we phase at this period, we can obtain a light curve of the candidate variable star (see Figure 3.1, bottom). The amplitude of the light curve was determined by the Fourier fit, yielding 0.05 mag.

Muñoz et al. (2018) found that the star #5 (see in Figure 3.2 the red star) is the most metal-poor of the sample with [Fe/H]=-0.55 dex (see Table 3.3), which may be due to its variability, but all its chemical patterns show good agreement with the other members of NGC 6528.

Candidate Variable Star in NGC 6553: In the study described by Muñoz et al. (2019, in preparation) analyze seven stars to found their chemical abundances. In the star #6 (see Figure 3.6, the blue star) we detected a periodicity using aperture photometry from CASU. In total we obtained 70 epochs (see Figure 3.3, top left) in a range of 12.061< K_s <13.198 with a error of 0.01 mag from August 2011 to September 2015. In Figure 3.3 (bottom) we can see the light curve of the candidate variable star phased at the period 29.04823 days found through a strong peak in the Generalized Lomb-Scargle periodogram (see Figure 3.5, top right). The amplitude of the light curve was determined by the Fourier fit, yielding 0.6 mag.

Candidate Variable Star in NGC 6569: In the same way that the others clusters, Muñoz et al. (2019, in preparation) analyzed seven stars. We search for variability in each one of these stars, and we found in the star #3 (see Figure 3.6, the orange star) a variability through aperture photometry from CASU. We obtained 27 epochs (see Figure 3.5, top left) in the K_s band in a range of 14.616< K_s <14.694 with a error of 0.01 from September 2011 to September 2015. As shown in Figure 3.5 (top right) we detect a strong peak at 1.45517 days with the Generalized Lomb-Scargle periodogram. The Figure 3.5(bottom) shows the light curve of the candidate variable star phased at this period. The amplitude of the light curve was determined by the Fourier fit, yielding 0.06 mag.

We could not identify the type of variable, since it is difficult to classify variability type, due to the few features showed in Ks bands. (Catelan et al., 2013; Alonso-García et al., 2015).

Table 3.1 Properties of the variable candidates

VVV ID	Globular Cluster	RA (J2000,h:m:s)	DEC (J2000,d:m:s)	Period (days)	A_{K_s} (mag)
VVV 515551240568	NGC 6528	18:04:45.38	-30:03:46.94	0.25729	0.05
VVV 515478094263	NGC 6553	18:09:23.98	-25:52:01.20	29.04823	0.6
VVV 515568658672	NGC 6569	18:13:37.98	-31:50:31.60	1.45517	0.06

Note. The properties of the variable candidates were estimated in the Section 3.3. Period (days) estimated using Generalized Lomb Scargle and Phase Dispersion Minimization, A_{K_s} (mag) is the amplitude of K_s magnitude determined through the Fourier fits.

Table 3.2 Photometric parameters

VVV ID	Z (mag)	Y (mag)	J (mag)	H (mag)	K_s (mag)
VVV 515551240568	13.00	12.50	11.87	10.95	10.68
VVV 515478094263	-	12.69	12.07	11.22	10.95
VVV 515568658672	14.91	14.53	14.04	13.30	13.15

Note. The Z and Y magnitudes are aperture photometry from VVV survey. The J,H and Ks magnitudes are de-reddened PSF photometry of VVV survey (Mauro et al., 2014; Cohen et al., 2017).

Table 3.3 Stellar Parameters

ID Cluster	Globular	VVV ID	RV_H (km s^{-1})	T_{eff} [K]	[Fe/H] dex	v_t [km/s]
5	NGC 6528$^{(1)}$	VVV 515551240568	209.70±0.23	4118	-0.55	1.79
6	NGC 6553$^{(2)}$	VVV 515478094263	-2.76±0.26	4399	-0.08	0.97
3	NGC 6569$^{(2)}$	VVV 515568658672	-52.57±0.41	4761	-0.62	0.84

Note. RV_H is the heliocentric radial velocity, T_{eff} is the effective temperature, [Fe/H] the metallicity and v_t is micro-turbulent velocity. These parameters were estimated by (1) Muñoz et al. (2018) and (2) Muñoz et al. (2019, in preparation).

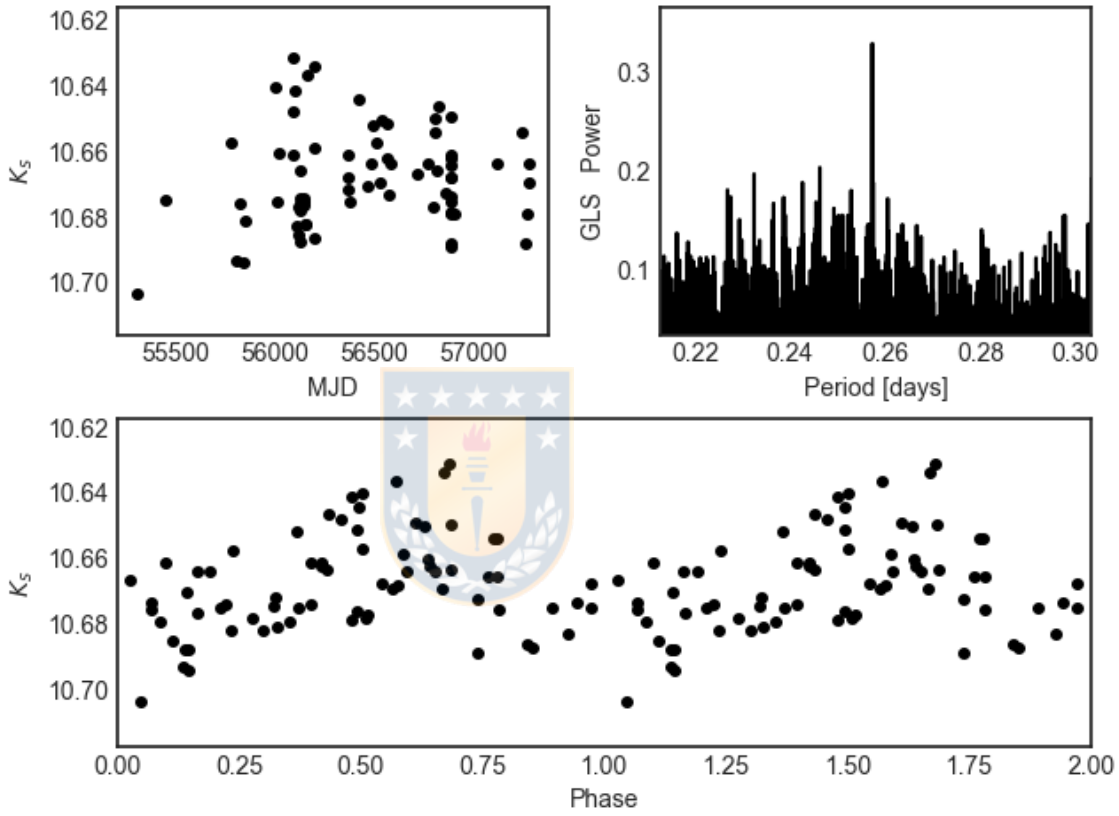

Figure 3.1 Candidate variable star of the globular cluster NGC6528. Top left: Light curve of the candidate variable star. Top right: Generalized Lomb-Scargle periodogram shows a strong peak at 0.25729 days. Bottom: Phased light curve of the candidate variable star. Source: Muñoz et al. (2018).

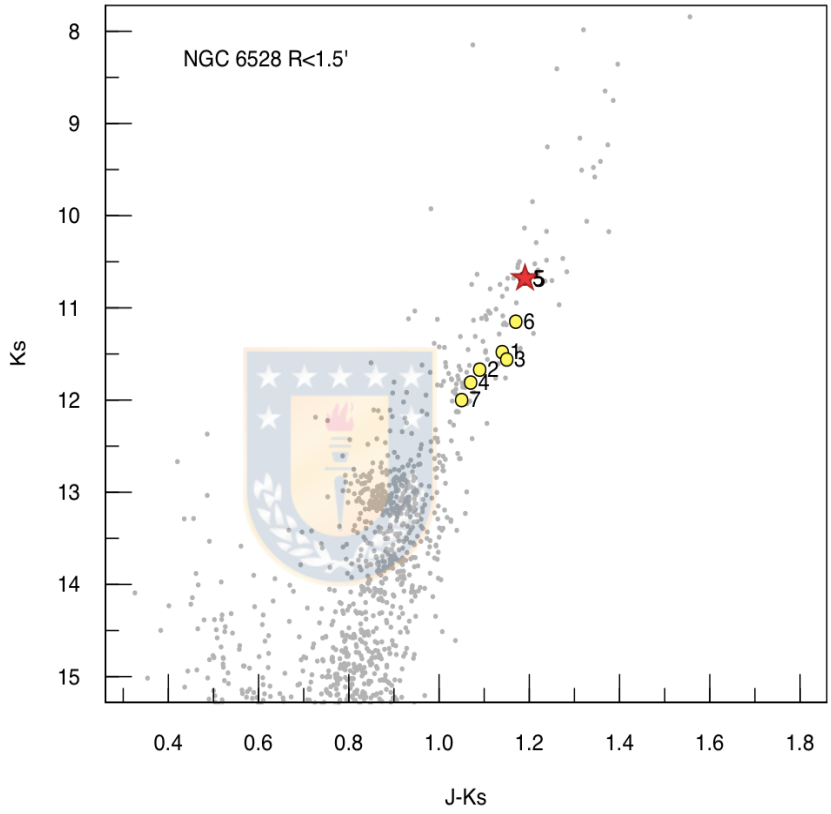

Figure 3.2 CMD of NGC 6528 from the VVV survey corrected by the VVV reddening maps (Gonzalez et al., 2012). The yellow filled circles are our observed UVES sample. The red star is the candidate variable star. Source: Muñoz et al. (2018).

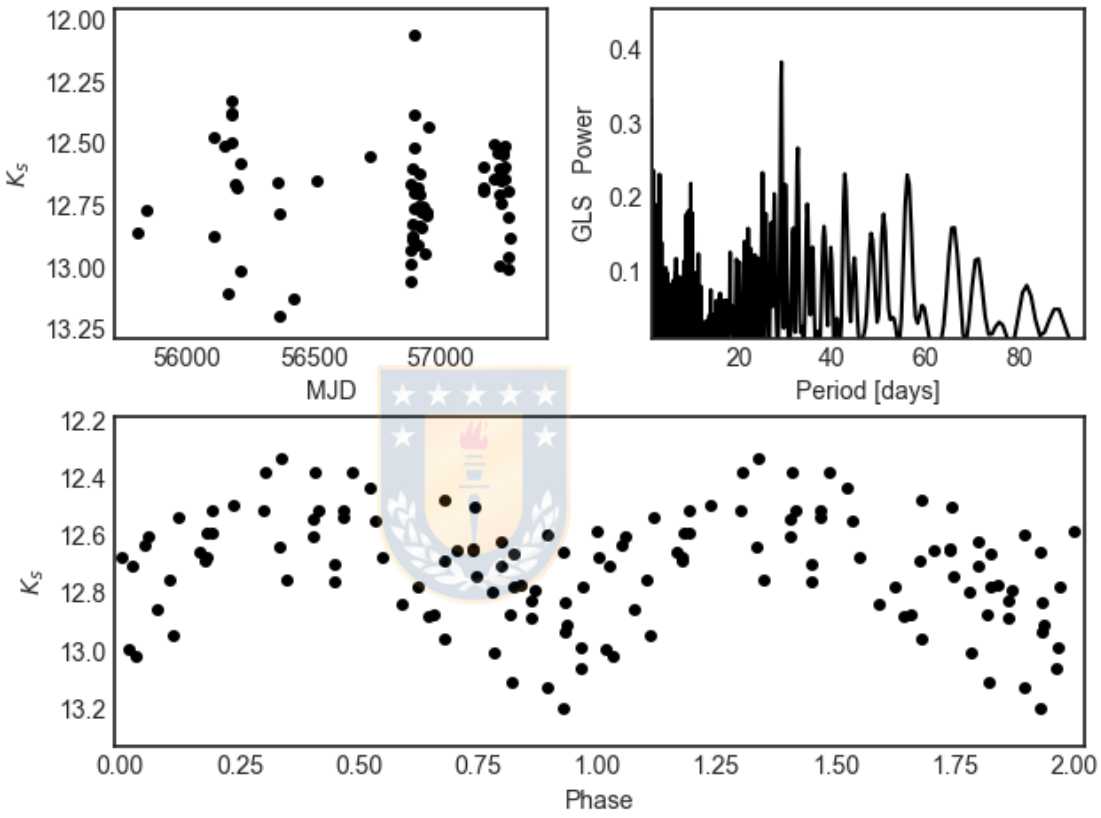

Figure 3.3 Candidate variable star of the globular cluster NGC6553. Top left: Light curve of the candidate variable star. Top right: Generalized Lomb-Scargle periodogram shows a strong peak at 29.04823 days. Bottom: Phased light curve of the candidate variable star. Source: Muñoz et al. (2019, in preparation).

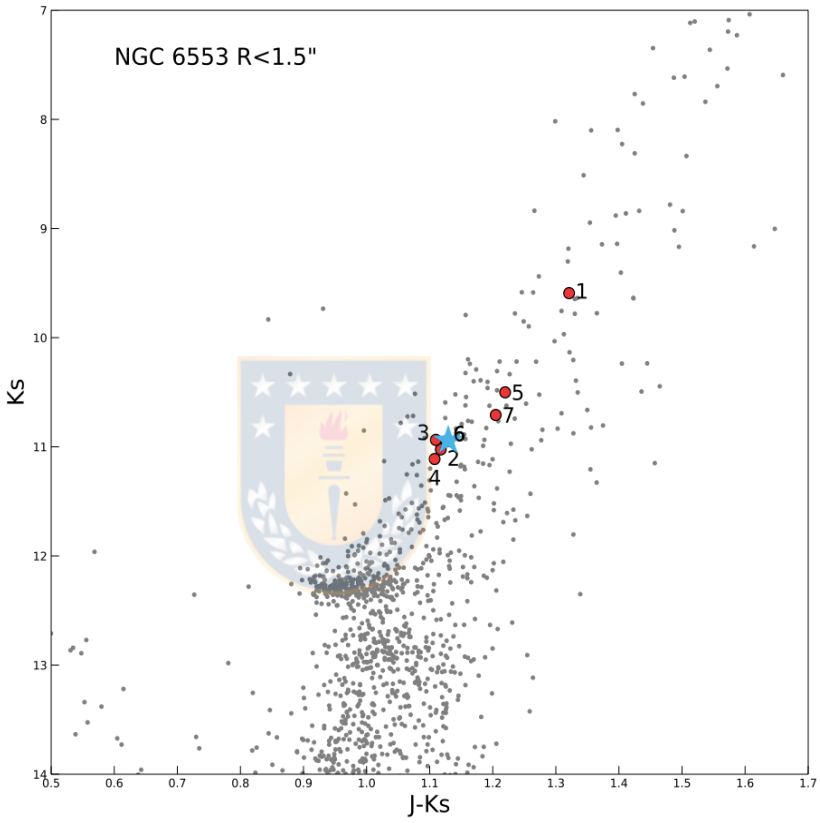

Figure 3.4 CMD of NGC 6553 from the VVV survey corrected by the VVV reddening maps (Gonzalez et al., 2012). The red filled circles are our observed UVES sample. The blue star is the candidate variable star. Source: Muñoz et al. (2019, in preparation).

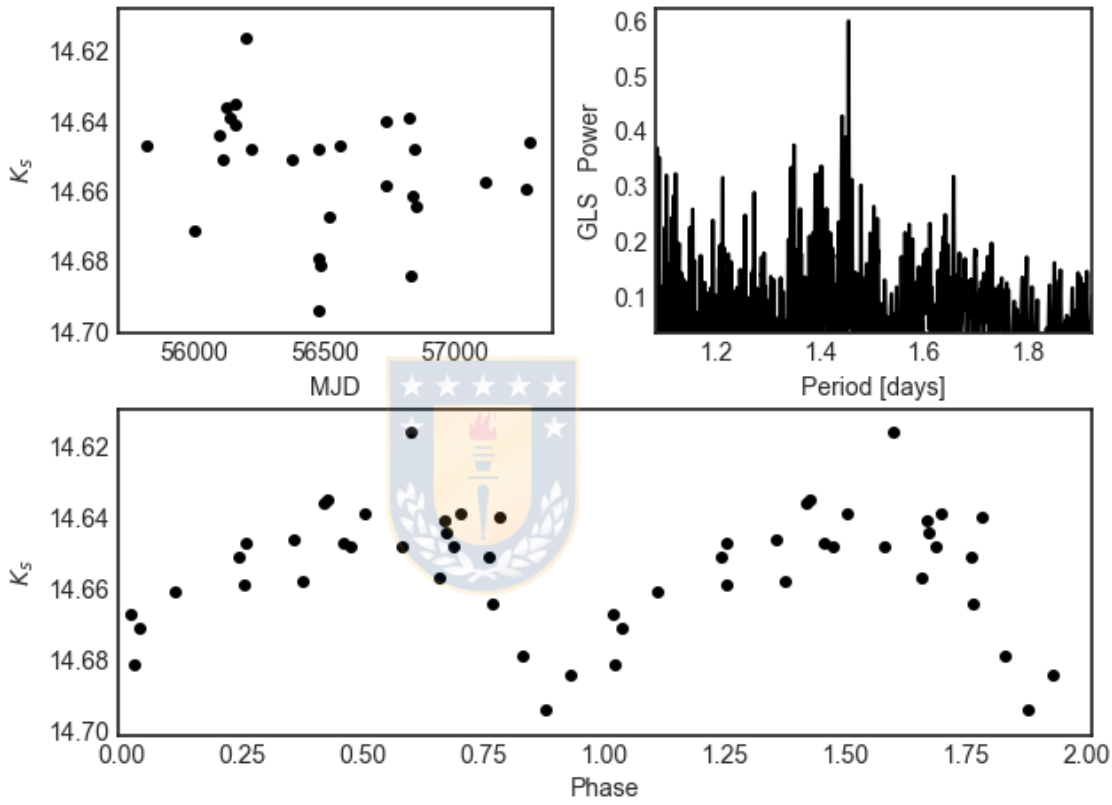

Figure 3.5 Candidate variable star of the globular cluster NGC6569. Top left: Light curve of the candidate variable star. Top right: Generalized Lomb-Scargle periodogram shows a strong peak at 1.45517 days. Bottom: Phased light curve of the candidate variable star. Source: Muñoz et al. (2019, in preparation).

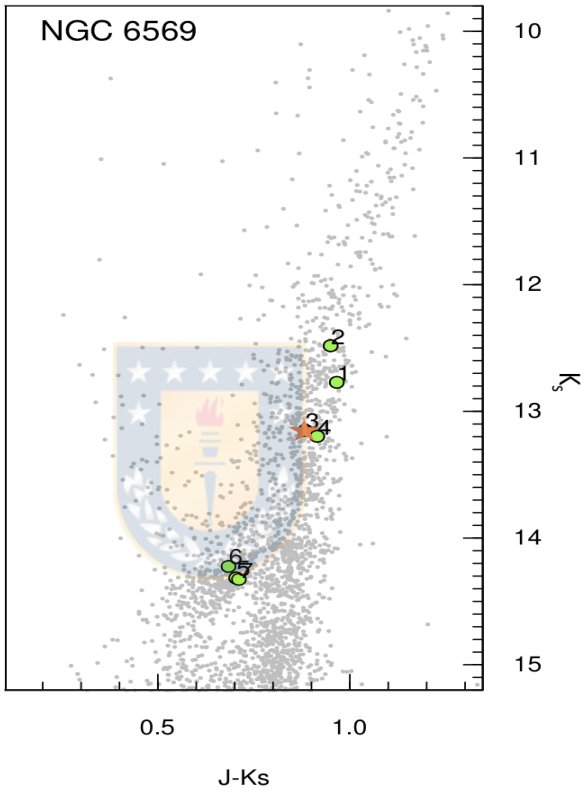

Figure 3.6 CMD of NGC 6569 from the VVV survey corrected by the VVV reddening maps (Gonzalez et al., 2012). The red filled circles are our observed UVES sample. The orange star is the candidate variable star. Source: Muñoz et al. (2019, in preparation).

4

Summary

4.1 Search for Exoplanetary Transits

We reported the discovery of five exoplanet candidates detected in the Galactic Bulge with K2 data with orbital periods between 3.6390 and 35.1695 days and planetary radii in the range of 2.0 to 48.1 $R_{\oplus}$. These planet candidates orbit host stars with a range of magnitudes and temperatures (12.039 < K_p < 16.072, and 4184 K < T_{eff} <4647 K).

Two of our candidates were classified as stellar objects (224439122 and 224560837) and two as low mass planets (227560005 and 230778501) according to Hatzes & Rauer (2015), but we considered that 224439122 and 224560837 passed the test to discard false positive mentioned in Section 2.3, therefore there are the possibility that these targets could be planets. Due to the radius for the host star of the candidate 231635524 is not available in Gaia DR2, we can not estimate the planetary radius, and consequently, we can not predict the mass of the planet. Therefore, as we explained in Section 2.5, we infer that the candidate 231635524 could be a giant gaseous planet.

4.2 Search for Variability in Bulge Globular Clusters

Muñoz et al. (2018) and Muñoz et al. (2019, in preparation) analyzed the behavior of three Bulge Globular Cluster associated with the Multiple Populations phenomenon. For this reason, he obtained chemical abundance of Red Giant Branch (RGB) stars using high-resolution spectroscopy from FLAMES-UVES. Thanks to the VVV survey, we search for variability in stars belonging to the Bulge Globular Clusters: NGC 6528, NGC 6553 and NGC 6569 and we detected in each of these one candidate variable star with a period of 0.25729, 29.04823 and 1.45517 days, respectively. The iron abundance of the stars used to study these clusters are in good agreement with previous studies, expect for the candidate variable stars of the cluster NGC 6528, it is the most metal poor of the sample.

4.3 Outlook

4.3.1 Follow-up Spectroscopic Observations

Through the transit method, we can obtain the planetary radius, but we need the stellar radius, which was estimated using Gaia DR2. It is necessary to estimate the masses to classify our exoplanet candidates. Because we can not measure the mass with this technique, we predict the mass of the planet using Forecaster Python package, which uses a mass-radius relationship. Even though these parameters are not highly accurate, they represent a good initial estimate to perform our analysis and give a preliminary idea about the nature of our candidates. Therefore, we would like to encourage follow-up spectroscopic observations in order to confirm our exoplanet candidates and to refine their physical parameters.

4.3.2 Relationship between variability and metallicity?

We search for variability in Bulge Globular Clusters that were part of the study of Muñoz et al. (2018) and Muñoz et al. (2019, in preparation). We found that the candidate variable star belonging to the globular cluster NGC 6528 is most metal-poor of the sample. We thought that probably this discrepancy is due to the variability.

Therefore, we would like to take spectroscopic data in different phases of the candidate variable star to understand if indeed this is the cause or not. Also, we would like to search for variability in all the stars of this globular cluster. Probably, the stars around the metal-poor candidate variable star have the same characteristics.

These are some questions that arise in this study, taking into account that the candidate variable stars found in NGC 6553 and NGC 6569 do not show this effect.

Bibliography

Abadi, M. G., Navarro, J. F., Steinmetz, M., & Eke, V. R., *ApJ*, 591:499–514, July 2003.

Adams, E. R., Jackson, B., & Endl, M., *AJ*, 152:47, August 2016.

Alonso, R., Brown, T. M., Torres, G., Latham, D. W., Sozzetti, A., Mandushev, G., Belmonte, J. A., Charbonneau, D., Deeg, H. J., Dunham, E. W., O'Donovan, F. T., & Stefanik, R. P., *ApJ*, 613:L153–L156, October 2004.

Alonso-García, J., Dékány, I., Catelan, M., Contreras Ramos, R., Gran, F., Amigo, P., Leyton, P., & Minniti, D., *AJ*, 149:99, March 2015.

Alsubai, K. A., Parley, N. R., Bramich, D. M., Horne, K., Collier Cameron, A., West, R. G., Sorensen, P. M., Pollacco, D., Smith, J. C., & Fors, O., , 63:465–480, December 2013.

Andrae, R., Fouesneau, M., Creevey, O., Ordenovic, C., Mary, N., Burlacu, A., Chaoul, L., Jean-Antoine-Piccolo, A., Kordopatis, G., Korn, A., Lebreton, Y., Panem, C., Pichon, B., Thévenin, F., Walmsley, G., & Bailer-Jones, C. A. L., *A&A*, 616:A8, August 2018.

Armitage, P. J. *Astrophysics of Planet Formation*. 2010.

Athanassoula, E., *MNRAS*, 358:1477–1488, April 2005.

Bailer-Jones, C. A. L., Rybizki, J., Fouesneau, M., Mantelet, G., & Andrae, R., *AJ*, 156: 58, August 2018.

Bakos, G., Noyes, R. W., Kovács, G., Stanek, K. Z., Sasselov, D. D., & Domsa, I., *PASP*, 116:266–277, March 2004.

Barge, P., Baglin, A., Auvergne, M., & CoRoT Team. *CoRoT: pioneer space mission for exoplanet transit search*. In Sun, Y.-S., Ferraz-Mello, S., & Zhou, J.-L., editors, *Exo-*

planets: Detection, Formation and Dynamics, volume 249 of *IAU Symposium*, pages 3–16, May 2008. doi: 10.1017/S1743921308016293.

Barros, S. C. C., Demangeon, O., & Deleuil, M., *A&A*, 594:A100, October 2016.

Bond, I. A., Abe, F., Dodd, R. J., Hearnshaw, J. B., Honda, M., Jugaku, J., Kilmartin, P. M., Marles, A., Masuda, K., Matsubara, Y., Muraki, Y., Nakamura, T., Nankivell, G., Noda, S., Noguchi, C., Ohnishi, K., Rattenbury, N. J., Reid, M., Saito, T., Sato, H., Sekiguchi, M., Skuljan, J., Sullivan, D. J., Sumi, T., Takeuti, M., Watase, Y., Wilkinson, S., Yamada, R., Yanagisawa, T., & Yock, P. C. M., *MNRAS*, 327:868–880, November 2001.

Bond, I. A., Udalski, A., Jaroszyński, M., Rattenbury, N. J., Paczyński, B., Soszyński, I., Wyrzykowski, L., Szymański, M. K., Kubiak, M., Szewczyk, O., Żebruń, K., Pietrzyński, G., Abe, F., Bennett, D. P., Eguchi, S., Furuta, Y., Hearnshaw, J. B., Kamiya, K., Kilmartin, P. M., Kurata, Y., Masuda, K., Matsubara, Y., Muraki, Y., Noda, S., Okajima, K., Sako, T., Sekiguchi, T., Sullivan, D. J., Sumi, T., Tristram, P. J., Yanagisawa, T., Yock, P. C. M., & OGLE Collaboration, *ApJ*, 606:L155–L158, May 2004.

Borucki, W. J., Koch, D., Basri, G., Batalha, N., Brown, T., Caldwell, D., Caldwell, J., Christensen-Dalsgaard, J., Cochran, W. D., DeVore, E., Dunham, E. W., Dupree, A. K., Gautier, T. N., Geary, J. C., Gilliland, R., Gould, A., Howell, S. B., Jenkins, J. M., Kondo, Y., Latham, D. W., Marcy, G. W., Meibom, S., Kjeldsen, H., Lissauer, J. J., Monet, D. G., Morrison, D., Sasselov, D., Tarter, J., Boss, A., Brownlee, D., Owen, T., Buzasi, D., Charbonneau, D., Doyle, L., Fortney, J., Ford, E. B., Holman, M. J., Seager, S., Steffen, J. H., Welsh, W. F., Rowe, J., Anderson, H., Buchhave, L., Ciardi, D., Walkowicz, L., Sherry, W., Horch, E., Isaacson, H., Everett, M. E., Fischer, D., Torres, G., Johnson, J. A., Endl, M., MacQueen, P., Bryson, S. T., Dotson, J., Haas, M., Kolodziejczak, J., Van Cleve, J., Chandrasekaran, H., Twicken, J. D., Quintana,

E. V., Clarke, B. D., Allen, C., Li, J., Wu, H., Tenenbaum, P., Verner, E., Bruhweiler, F., Barnes, J., & Prsa, A., *Science*, 327:977, February 2010a.

Borucki, W. J., Koch, D., Basri, G., Batalha, N., Brown, T., Caldwell, D., Caldwell, J., Christensen-Dalsgaard, J., Cochran, W. D., DeVore, E., Dunham, E. W., Dupree, A. K., Gautier, T. N., Geary, J. C., Gilliland, R., Gould, A., Howell, S. B., Jenkins, J. M., Kondo, Y., Latham, D. W., Marcy, G. W., Meibom, S., Kjeldsen, H., Lissauer, J. J., Monet, D. G., Morrison, D., Sasselov, D., Tarter, J., Boss, A., Brownlee, D., Owen, T., Buzasi, D., Charbonneau, D., Doyle, L., Fortney, J., Ford, E. B., Holman, M. J., Seager, S., Steffen, J. H., Welsh, W. F., Rowe, J., Anderson, H., Buchhave, L., Ciardi, D., Walkowicz, L., Sherry, W., Horch, E., Isaacson, H., Everett, M. E., Fischer, D., Torres, G., Johnson, J. A., Endl, M., MacQueen, P., Bryson, S. T., Dotson, J., Haas, M., Kolodziejczak, J., Van Cleve, J., Chandrasekaran, H., Twicken, J. D., Quintana, E. V., Clarke, B. D., Allen, C., Li, J., Wu, H., Tenenbaum, P., Verner, E., Bruhweiler, F., Barnes, J., & Prsa, A., *Science*, 327:977, February 2010b.

Borucki, W. J., Koch, D. G., Basri, G., Batalha, N., Boss, A., Brown, T. M., Caldwell, D., Christensen-Dalsgaard, J., Cochran, W. D., DeVore, E., Dunham, E. W., Dupree, A. K., Gautier, III, T. N., Geary, J. C., Gilliland, R., Gould, A., Howell, S. B., Jenkins, J. M., Kjeldsen, H., Latham, D. W., Lissauer, J. J., Marcy, G. W., Monet, D. G., Sasselov, D., Tarter, J., Charbonneau, D., Doyle, L., Ford, E. B., Fortney, J., Holman, M. J., Seager, S., Steffen, J. H., Welsh, W. F., Allen, C., Bryson, S. T., Buchhave, L., Chandrasekaran, H., Christiansen, J. L., Ciardi, D., Clarke, B. D., Dotson, J. L., Endl, M., Fischer, D., Fressin, F., Haas, M., Horch, E., Howard, A., Isaacson, H., Kolodziejczak, J., Li, J., MacQueen, P., Meibom, S., Prsa, A., Quintana, E. V., Rowe, J., Sherry, W., Tenenbaum, P., Torres, G., Twicken, J. D., Van Cleve, J., Walkowicz, L., & Wu, H., *ApJ*, 728:117, February 2011.

Broeg, C., Fortier, A., Ehrenreich, D., Alibert, Y., Baumjohann, W., Benz, W., Deleuil, M., Gillon, M., Ivanov, A., Liseau, R., Meyer, M., Oloffson, G., Pagano, I., Piotto, G., Pollacco, D., Queloz, D., Ragazzoni, R., Renotte, E., Steller, M., & Thomas, N.

CHEOPS: A transit photometry mission for ESA's small mission programme. In *European Physical Journal Web of Conferences*, volume 47 of *European Physical Journal Web of Conferences*, page 03005, April 2013. doi: 10.1051/epjconf/20134703005.

Buchhave, L. A., Bizzarro, M., Latham, D. W., Sasselov, D., Cochran, W. D., Endl, M., Isaacson, H., Juncher, D., & Marcy, G. W., *Nature*, 509:593–595, May 2014.

Cameron, P. B., Britton, M. C., & Kulkarni, S. R., *AJ*, 137:83–93, January 2009.

Campbell, B., Walker, G. A. H., & Yang, S., *ApJ*, 331:902–921, August 1988.

Cardelli, J. A., Clayton, G. C., & Mathis, J. S., *ApJ*, 345:245–256, October 1989.

Catelan, M., Minniti, D., Lucas, P. W., Dékány, I., Saito, R. K., Angeloni, R., Alonso-García, J., Hempel, M., Helminiak, K., Jordán, A., Contreras Ramos, R., Navarrete, C., Beamín, J. C., Rojas, A. F., Gran, F., Ferreira Lopes, C. E., Contreras Peña, C., Kerins, E., Huckvale, L., Rejkuba, M., Cohen, R., Mauro, F., Borissova, J., Amigo, P., Eyheramendy, S., Pichara, K., Espinoza, N., Navarro, C., Hajdu, G., Calderón Espinoza, D. N., Muro, G. A., Andrews, H., Motta, V., Kurtev, R., Emerson, J. P., Moni Bidin, C., & Chené, A.-N., *arXiv e-prints*, October 2013.

Cescutti, G., Chiappini, C., & Hirschi, R. *The oldest stars of the bulge: new information on the ancient Galaxy*. In Chiappini, C., Minchev, I., Starkenburg, E., & Valentini, M., editors, *Rediscovering Our Galaxy*, volume 334 of *IAU Symposium*, pages 94–97, August 2018. doi: 10.1017/S1743921317008183.

Charbonneau, D., Brown, T. M., Latham, D. W., & Mayor, M., *ApJ*, 529:L45–L48, January 2000.

Chauvin, G., Lagrange, A.-M., Dumas, C., Zuckerman, B., Mouillet, D., Song, I., Beuzit, J.-L., & Lowrance, P., *A&A*, 425:L29–L32, October 2004.

Chazelas, B., Pollacco, D., Queloz, D., Rauer, H., Wheatley, P. J., West, R., Da Silva Bento, J., Burleigh, M., McCormac, J., Eigmüller, P., Erikson, A., Genolet, L., Goad,

M., Jordán, A., Neveu, M., & Walker, S. *NGTS: a robotic transit survey to detect Neptune and super-Earth mass planets*. In *Ground-based and Airborne Telescopes IV*, volume 8444 of *Proc. SPIE*, page 84440E, September 2012. doi: 10.1117/12.925755.

Chen, J. & Kipping, D., *ApJ*, 834:17, January 2017.

Cohen, R. E., Moni Bidin, C., Mauro, F., Bonatto, C., & Geisler, D., *MNRAS*, 464:1874–1902, January 2017.

Contreras Peña, C., Catelan, M., Grundahl, F., Stephens, A. W., & Smith, H. A., *AJ*, 155: 116, March 2018.

Contreras Ramos, R., Minniti, D., Fernández-Trincado, J. G., Alonso-García, J., Catelan, M., Gran, F., Hajdu, G., Hanke, M., Hempel, M., Moreno Díaz, E., Pérez-Villegas, Á., Rojas-Arriagada, Á., & Zoccali, M., *ApJ*, 863:78, August 2018.

Crossfield, I. J. M., Guerrero, N., David, T., Quinn, S. N., Feinstein, A. D., Huang, C., Yu, L., Collins, K. A., Fulton, B. J., Benneke, B., Peterson, M., Bieryla, A., Schlieder, J. E., Kosiarek, M. R., Bristow, M., Newton, E., Bedell, M., Latham, D. W., Christiansen, J. L., Esquerdo, G. A., Berlind, P., Calkins, M. L., Shporer, A., Burt, J., Ballard, S., Rodriguez, J. E., Mehrle, N., Seager, S., Dittmann, J., Berardo, D., Sha, L., Essack, Z., Zhan, Z., Owens, M., Kain, I., Livingston, J. H., Petigura, E. A., Dressing, C. D., Gonzales, E. J., Isaacson, H., & Howard, A. W., *ArXiv e-prints*, June 2018.

Cumming, A., Marcy, G. W., & Butler, R. P., *ApJ*, 526:890–915, December 1999.

Cutri, R. M., Skrutskie, M. F., van Dyk, S., Beichman, C. A., Carpenter, J. M., Chester, T., Cambresy, L., Evans, T., Fowler, J., Gizis, J., Howard, E., Huchra, J., Jarrett, T., Kopan, E. L., Kirkpatrick, J. D., Light, R. M., Marsh, K. A., McCallon, H., Schneider, S., Stiening, R., Sykes, M., Weinberg, M., Wheaton, W. A., Wheelock, S., & Zacarias, N., *VizieR Online Data Catalog*, 2246, June 2003.

Dai, X. & Guerras, E., *ApJ*, 853:L27, February 2018.

Donnison, J. R., *MNRAS*, 406:1918–1934, August 2010.

Dressing, C. D., Newton, E. R., Schlieder, J. E., Charbonneau, D., Knutson, H. A., Vanderburg, A., & Sinukoff, E., *ApJ*, 836:167, February 2017a.

Dressing, C. D., Vanderburg, A., Schlieder, J. E., Crossfield, I. J. M., Knutson, H. A., Newton, E. R., Ciardi, D. R., Fulton, B. J., Gonzales, E. J., Howard, A. W., Isaacson, H., Livingston, J., Petigura, E. A., Sinukoff, E., Everett, M., Horch, E., & Howell, S. B., *AJ*, 154:207, November 2017b.

Elmegreen, B. G., *ApJ*, 517:103–107, May 1999.

Figuera Jaimes, R., Bramich, D. M., Kains, N., Skottfelt, J., Jørgensen, U. G., Horne, K., Dominik, M., Alsubai, K. A., Bozza, V., Burgdorf, M. J., Calchi Novati, S., Ciceri, S., D'Ago, G., Evans, D. F., Galianni, P., Gu, S.-H., Harpsøe, K. B. W., Haugbølle, T., Hinse, T. C., Hundertmark, M., Juncher, D., Kerins, E., Korhonen, H., Kuffmeier, M., Mancini, L., Peixinho, N., Popovas, A., Rabus, M., Rahvar, S., Scarpetta, G., Schmidt, R. W., Snodgrass, C., Southworth, J., Starkey, D., Street, R. A., Surdej, J., Tronsgaard, R., Unda-Sanzana, E., von Essen, C., Wang, X.-B., Wertz, O., & MiNDSTEp Consortium, *A&A*, 592:A120, August 2016.

Fischer, D., Driscoll, P., Isaacson, H., Giguere, M., Marcy, G. W., Valenti, J., Wright, J. T., Henry, G. W., Johnson, J. A., Howard, A., Peek, K., & McCarthy, C., *ApJ*, 703: 1545–1556, October 2009.

Fischer, D. A., Howard, A. W., Laughlin, G. P., Macintosh, B., Mahadevan, S., Sahlmann, J., & Yee, J. C., *Protostars and Planets VI*, pages 715–737, 2014.

Foreman-Mackey, D., Hogg, D. W., Lang, D., & Goodman, J., *PASP*, 125:306–312, 2013.

Gaia Collaboration, Prusti, T., de Bruijne, J. H. J., Brown, A. G. A., Vallenari, A., Babusiaux, C., Bailer-Jones, C. A. L., Bastian, U., Biermann, M., Evans, D. W., & et al., *A&A*, 595:A1, November 2016.

Gaia Collaboration, Brown, A. G. A., Vallenari, A., Prusti, T., de Bruijne, J. H. J., Babusiaux, C., Bailer-Jones, C. A. L., Biermann, M., Evans, D. W., Eyer, L., & et al., *A&A*, 616:A1, August 2018.

Gonzalez, O. A., Rejkuba, M., Zoccali, M., Valenti, E., Minniti, D., Schultheis, M., Tobar, R., & Chen, B., *A&A*, 543:A13, July 2012.

Gonzalez, O. A., Rejkuba, M., Zoccali, M., Valent, E., Minniti, D., & Tobar, R., *A&A*, 552:A110, April 2013.

Goodman, J. & Weare, J., *Communications in Applied Mathematics and Computational Science, Vol. 5, No. 1, p. 65-80, 2010*, 5:65–80, 2010.

Gran, F., Minniti, D., Saito, R. K., Navarrete, C., Dékány, I., McDonald, I., Contreras Ramos, R., & Catelan, M., *A&A*, 575:A114, March 2015.

Hatzes, A. P. & Rauer, H., *ApJ*, 810:L25, September 2015.

Hatzes, A. P., Cochran, W. D., Endl, M., McArthur, B., Paulson, D. B., Walker, G. A. H., Campbell, B., & Yang, S., *ApJ*, 599:1383–1394, December 2003.

Henden, A. A., Templeton, M., Terrell, D., Smith, T. C., Levine, S., & Welch, D., *VizieR Online Data Catalog*, 2336, January 2016.

Henderson, C. B. & Stassun, K. G., *ApJ*, 747:51, March 2012.

Henderson, C. B., Poleski, R., Penny, M., Street, R. A., Bennett, D. P., Hogg, D. W., Gaudi, B. S., K2 Campaign 9 Microlensing Science Team, Zhu, W., Barclay, T., Barentsen, G., Howell, S. B., Mullally, F., Udalski, A., Szymański, M. K., Skowron, J., Mróz, P., Kozłowski, S., Wyrzykowski, Ł., Pietrukowicz, P., Soszyński, I., Ulaczyk, K., Pawlak, M., OGLE Project, T., Sumi, T., Abe, F., Asakura, Y., Barry, R. K., Bhattacharya, A., Bond, I. A., Donachie, M., Freeman, M., Fukui, A., Hirao, Y., Itow, Y., Koshimoto, N., Li, M. C. A., Ling, C. H., Masuda, K., Matsubara, Y., Muraki, Y.,

Nagakane, M., Ohnishi, K., Oyokawa, H., Rattenbury, N., Saito, T., Sharan, A., Sullivan, D. J., Tristram, P. J., Yonehara, A., MOA Collaboration, Bachelet, E., Bramich, D. M., Cassan, A., Dominik, M., Figuera Jaimes, R., Horne, K., Hundertmark, M., Mao, S., Ranc, C., Schmidt, R., Snodgrass, C., Steele, I. A., Tsapras, Y., Wambsganss, J., RoboNet Project, T., Bozza, V., Burgdorf, M. J., Jørgensen, U. G., Calchi Novati, S., Ciceri, S., D'Ago, G., Evans, D. F., Hessman, F. V., Hinse, T. C., Husser, T.-O., Mancini, L., Popovas, A., Rabus, M., Rahvar, S., Scarpetta, G., Skottfelt, J., Southworth, J., Unda-Sanzana, E., The MiNDSTEp Team, Bryson, S. T., Caldwell, D. A., Haas, M. R., Larson, K., McCalmont, K., Packard, M., Peterson, C., Putnam, D., Reedy, L., Ross, S., Van Cleve, J. E., K2C9 Engineering Team, Akeson, R., Batista, V., Beaulieu, J.-P., Beichman, C. A., Bryden, G., Ciardi, D., Cole, A., Coutures, C., Foreman-Mackey, D., Fouqué, P., Friedmann, M., Gelino, C., Kaspi, S., Kerins, E., Korhonen, H., Lang, D., Lee, C.-H., Lineweaver, C. H., Maoz, D., Marquette, J.-B., Mogavero, F., Morales, J. C., Nataf, D., Pogge, R. W., Santerne, A., Shvartzvald, Y., Suzuki, D., Tamura, M., Tisserand, P., & Wang, D., *PASP*, 128(12):124401, December 2016.

Henry, G. W., Marcy, G., Butler, R. P., & Vogt, S. S., *IAU Circ.*, 7307, November 1999.

Howard, C. D., Rich, R. M., Reitzel, D. B., Koch, A., De Propris, R., & Zhao, H., *ApJ*, 688:1060–1077, December 2008.

Johnson, M. C., Gandolfi, D., Fridlund, M., Csizmadia, S., Endl, M., Cabrera, J., Cochran, W. D., Deeg, H. J., Grziwa, S., Ramírez, I., Hatzes, A. P., Eigmüller, P., Barragán, O., Erikson, A., Guenther, E. W., Korth, J., Kuutma, T., Nespral, D., Pätzold, M., Palle, E., Prieto-Arranz, J., Rauer, H., & Saario, J., *AJ*, 151:171, June 2016.

Jones, H. R. A., Butler, R. P., Tinney, C. G., Marcy, G. W., Carter, B. D., Penny, A. J., McCarthy, C., & Bailey, J., *MNRAS*, 369:249–256, June 2006.

Kipping, D. M., *MNRAS*, 408:1758–1769, November 2010.

Kopal, Z., *Harvard College Observatory Circular*, 454:1–12, 1950.

Kovács, G., Zucker, S., & Mazeh, T., *A&A*, 391:369–377, August 2002.

Kreidberg, L., *PASP*, 127:1161, November 2015.

Kunder, A., Koch, A., Rich, R. M., de Propris, R., Howard, C. D., Stubbs, S. A., Johnson, C. I., Shen, J., Wang, Y., Robin, A. C., Kormendy, J., Soto, M., Frinchaboy, P., Reitzel, D. B., Zhao, H., & Origlia, L., *AJ*, 143:57, March 2012.

Lazorenko, P. F. & Lazorenko, G. A., *A&A*, 427:1127–1143, December 2004.

Lenzen, R., Hartung, M., Brandner, W., Finger, G., Hubin, N. N., Lacombe, F., Lagrange, A.-M., Lehnert, M. D., Moorwood, A. F. M., & Mouillet, D. *NAOS-CONICA first on sky results in a variety of observing modes*. In Iye, M. & Moorwood, A. F. M., editors, *Instrument Design and Performance for Optical/Infrared Ground-based Telescopes*, volume 4841 of *Proc. SPIE*, pages 944–952, March 2003. doi: 10.1117/12.460044.

Livingston, J. H., Endl, M., Dai, F., Cochran, W. D., Barragan, O., Gandolfi, D., Hirano, T., Grziwa, S., Smith, A. M. S., Albrecht, S., Cabrera, J., Csizmadia, S., de Leon, J. P., Deeg, H., Eigmüller, P., Erikson, A., Everett, M., Fridlund, M., Fukui, A., Guenther, E. W., Hatzes, A. P., Howell, S., Korth, J., Narita, N., Nespral, D., Nowak, G., Palle, E., Pätzold, M., Persson, C. M., Prieto-Arranz, J., Rauer, H., Tamura, M., Van Eylen, V., & Winn, J. N., *AJ*, 156:78, August 2018.

Lomb, N. R., *Ap&SS*, 39:447–462, February 1976.

Macintosh, B., Graham, J. R., Barman, T., De Rosa, R. J., Konopacky, Q., Marley, M. S., Marois, C., Nielsen, E. L., Pueyo, L., Rajan, A., Rameau, J., Saumon, D., Wang, J. J., Patience, J., Ammons, M., Arriaga, P., Artigau, E., Beckwith, S., Brewster, J., Bruzzone, S., Bulger, J., Burningham, B., Burrows, A. S., Chen, C., Chiang, E., Chilcote, J. K., Dawson, R. I., Dong, R., Doyon, R., Draper, Z. H., Duchêne, G., Esposito, T. M., Fabrycky, D., Fitzgerald, M. P., Follette, K. B., Fortney, J. J., Gerard, B., Goodsell, S.,

Greenbaum, A. Z., Hibon, P., Hinkley, S., Cotten, T. H., Hung, L.-W., Ingraham, P., Johnson-Groh, M., Kalas, P., Lafreniere, D., Larkin, J. E., Lee, J., Line, M., Long, D., Maire, J., Marchis, F., Matthews, B. C., Max, C. E., Metchev, S., Millar-Blanchaer, M. A., Mittal, T., Morley, C. V., Morzinski, K. M., Murray-Clay, R., Oppenheimer, R., Palmer, D. W., Patel, R., Perrin, M. D., Poyneer, L. A., Rafikov, R. R., Rantakyrö, F. T., Rice, E. L., Rojo, P., Rudy, A. R., Ruffio, J.-B., Ruiz, M. T., Sadakuni, N., Saddlemyer, L., Salama, M., Savransky, D., Schneider, A. C., Sivaramakrishnan, A., Song, I., Soummer, R., Thomas, S., Vasisht, G., Wallace, J. K., Ward-Duong, K., Wiktorowicz, S. J., Wolff, S. G., & Zuckerman, B., *Science*, 350:64–67, October 2015.

Macintosh, B. A., Anthony, A., Atwood, J., Barriga, N., Bauman, B., Caputa, K., Chilcote, J., Dillon, D., Doyon, R., Dunn, J., Gavel, D. T., Galvez, R., Goodsell, S. J., Graham, J. R., Hartung, M., Isaacs, J., Kerley, D., Konopacky, Q., Labrie, K., Larkin, J. E., Maire, J., Marois, C., Millar-Blanchaer, M., Nunez, A., Oppenheimer, B. R., Palmer, D. W., Pazder, J., Perrin, M., Poyneer, L. A., Quirez, C., Rantakyro, F., Reshtov, V., Saddlemyer, L., Sadakuni, N., Savransky, D., Sivaramakrishnan, A., Smith, M., Soummer, R., Thomas, S., Wallace, J. K., Weiss, J., & Wiktorowicz, S. *The Gemini Planet Imager: integration and status*. In *Ground-based and Airborne Instrumentation for Astronomy IV*, volume 8446 of *Proc. SPIE*, page 84461U, September 2012. doi: 10.1117/12.926721.

Marois, C., Macintosh, B., Barman, T., Zuckerman, B., Song, I., Patience, J., Lafrenière, D., & Doyon, R., *Science*, 322:1348, November 2008.

Martinazzi, E., Kepler, S. O., & Costa, J. E. S., *MNRAS*, 468:2816–2821, July 2017.

Mauro, F., Moni Bidin, C., Geisler, D., Saviane, I., Da Costa, G. S., Gormaz-Matamala, A. C., Vasquez, S., Chené, A.-N., Cohen, R., & Dias, B., *A&A*, 563:A76, March 2014.

Mayo, A. W., Vanderburg, A., Latham, D. W., Bieryla, A., Morton, T. D., Buchhave, L. A., Dressing, C. D., Beichman, C., Berlind, P., Calkins, M. L., Ciardi, D. R., Crossfield, I. J. M., Esquerdo, G. A., Everett, M. E., Gonzales, E. J., Hirsch, L. A., Horch,

E. P., Howard, A. W., Howell, S. B., Livingston, J., Patel, R., Petigura, E. A., Schlieder, J. E., Scott, N. J., Schumer, C. F., Sinukoff, E., Teske, J., & Winters, J. G., *AJ*, 155:136, March 2018.

Mayor, M. & Queloz, D., *Nature*, 378:355–359, November 1995.

Mayor, M., Pepe, F., Queloz, D., Bouchy, F., Rupprecht, G., Lo Curto, G., Avila, G., Benz, W., Bertaux, J.-L., Bonfils, X., Dall, T., Dekker, H., Delabre, B., Eckert, W., Fleury, M., Gilliotte, A., Gojak, D., Guzman, J. C., Kohler, D., Lizon, J.-L., Longinotti, A., Lovis, C., Megevand, D., Pasquini, L., Reyes, J., Sivan, J.-P., Sosnowska, D., Soto, R., Udry, S., van Kesteren, A., Weber, L., & Weilenmann, U., *The Messenger*, 114: 20–24, December 2003.

McArthur, B. E., Benedict, G. F., Barnes, R., Martioli, E., Korzennik, S., Nelan, E., & Butler, R. P., *ApJ*, 715:1203–1220, June 2010.

McCullough, P. R., Stys, J. E., Valenti, J. A., Fleming, S. W., Janes, K. A., & Heasley, J. N., *PASP*, 117:783–795, August 2005.

Minniti, D., Lucas, P. W., Emerson, J. P., Saito, R. K., Hempel, M., Pietrukowicz, P., Ahumada, A. V., Alonso, M. V., Alonso-Garcia, J., Arias, J. I., Bandyopadhyay, R. M., Barbá, R. H., Barbuy, B., Bedin, L. R., Bica, E., Borissova, J., Bronfman, L., Carraro, G., Catelan, M., Clariá, J. J., Cross, N., de Grijs, R., Dékány, I., Drew, J. E., Fariña, C., Feinstein, C., Fernández Lajús, E., Gamen, R. C., Geisler, D., Gieren, W., Goldman, B., Gonzalez, O. A., Gunthardt, G., Gurovich, S., Hambly, N. C., Irwin, M. J., Ivanov, V. D., Jordán, A., Kerins, E., Kinemuchi, K., Kurtev, R., López-Corredoira, M., Maccarone, T., Masetti, N., Merlo, D., Messineo, M., Mirabel, I. F., Monaco, L., Morelli, L., Padilla, N., Palma, T., Parisi, M. C., Pignata, G., Rejkuba, M., Roman-Lopes, A., Sale, S. E., Schreiber, M. R., Schröder, A. C., Smith, M., , Jr., L. S., Soto, M., Tamura, M., Tappert, C., Thompson, M. A., Toledo, I., Zoccali, M., & Pietrzynski, G., *New Astronomy*, 15:433–443, July 2010.

Minniti, D., Lucas, P., & VVV Team, *VizieR Online Data Catalog*, 2348, April 2017a.

Minniti, D., Palma, T., Dékány, I., Hempel, M., Rejkuba, M., Pullen, J., Alonso-García, J., Barbá, R., Barbuy, B., Bica, E., Bonatto, C., Borissova, J., Catelan, M., Carballo-Bello, J. A., Chene, A. N., Clariá, J. J., Cohen, R. E., Contreras Ramos, R., Dias, B., Emerson, J., Froebrich, D., Buckner, A. S. M., Geisler, D., Gonzalez, O. A., Gran, F., Hajdu, G., Irwin, M., Ivanov, V. D., Kurtev, R., Lucas, P. W., Majaess, D., Mauro, F., Moni-Bidin, C., Navarrete, C., Ramírez Alegría, S., Saito, R. K., Valenti, E., & Zoccali, M., *ApJ*, 838:L14, March 2017b.

Minniti, D., Schlafly, E. F., Palma, T., Clariá, J. J., Hempel, M., Alonso-García, J., Bica, E., Bonatto, C., Braga, V. F., Clementini, G., Garofalo, A., Gómez, M., Ivanov, V. D., Lucas, P. W., Pullen, J., Saito, R. K., & Smith, L. C., *ApJ*, 866:12, October 2018.

Montenegro, K., Minniti, D., Alonso-García, J., Hempel, M., Saito, R. K., Beers, T. C., & Brown, D., *arXiv e-prints*, September 2018.

Montet, B. T., Morton, T. D., Foreman-Mackey, D., Johnson, J. A., Hogg, D. W., Bowler, B. P., Latham, D. W., Bieryla, A., & Mann, A. W., *ApJ*, 809:25, August 2015.

Muñoz, C., Villanova, S., Geisler, D., Saviane, I., Dias, B., Cohen, R. E., & Mauro, F., *A&A*, 605:A12, August 2017.

Muñoz, C., Geisler, D., Villanova, S., Saviane, I., Cortés, C. C., Dias, B., Cohen, R. E., Mauro, F., & Moni Bidin, C., *ArXiv e-prints*, September 2018.

Navarro Molina, C., Borissova, J., Catelan, M., Alonso-García, J., Kerins, E., Kurtev, R., Lucas, P. W., Medina, N., Minniti, D., & Dékány, I., *MNRAS*, 462:1180–1191, October 2016.

Ness, M. & Lang, D., *AJ*, 152:14, July 2016.

Nishiyama, S., Nagata, T., Kusakabe, N., Matsunaga, N., Naoi, T., Kato, D., Nagashima, C., Sugitani, K., Tamura, M., Tanabé, T., & Sato, S., *ApJ*, 638:839–846, February 2006.

Norman, C. A., Sellwood, J. A., & Hasan, H., *ApJ*, 462:114, May 1996.

Park, B.-G., Kim, S.-L., Lee, J. W., Lee, B.-C., Lee, C.-U., Han, C., Kim, M., Moon, D.-S., Moon, H.-K., Rey, S.-C., Sung, E.-C., & Sung, H. *Korea Microlensing Telescope Network: science cases*. In *Ground-based and Airborne Telescopes IV*, volume 8444 of *Proc. SPIE*, page 844447, September 2012. doi: 10.1117/12.925826.

Pepe, F. A., Cristiani, S., Rebolo Lopez, R., Santos, N. C., Amorim, A., Avila, G., Benz, W., Bonifacio, P., Cabral, A., Carvas, P., Cirami, R., Coelho, J., Comari, M., Coretti, I., De Caprio, V., Dekker, H., Delabre, B., Di Marcantonio, P., D'Odorico, V., Fleury, M., García, R., Herreros Linares, J. M., Hughes, I., Iwert, O., Lima, J., Lizon, J.-L., Lo Curto, G., Lovis, C., Manescau, A., Martins, C., Mégevand, D., Moitinho, A., Molaro, P., Monteiro, M., Monteiro, M., Pasquini, L., Mordasini, C., Queloz, D., Rasilla, J. L., Rebordão, J. M., Santana Tschudi, S., Santin, P., Sosnowska, D., Spanò, P., Tenegi, F., Udry, S., Vanzella, E., Viel, M., Zapatero Osorio, M. R., & Zerbi, F. *ESPRESSO: the Echelle spectrograph for rocky exoplanets and stable spectroscopic observations*. In *Ground-based and Airborne Instrumentation for Astronomy III*, volume 7735 of *Proc. SPIE*, page 77350F, July 2010. doi: 10.1117/12.857122.

Pepper, J., Pogge, R. W., DePoy, D. L., Marshall, J. L., Stanek, K. Z., Stutz, A. M., Poindexter, S., Siverd, R., O'Brien, T. P., Trueblood, M., & Trueblood, P., *PASP*, 119: 923–935, August 2007.

Perryman, M. A. C., Lindegren, L., Kovalevsky, J., Hoeg, E., Bastian, U., Bernacca, P. L., Crézé, M., Donati, F., Grenon, M., Grewing, M., van Leeuwen, F., van der Marel, H., Mignard, F., Murray, C. A., Le Poole, R. S., Schrijver, H., Turon, C., Arenou, F., Froeschlé, M., & Petersen, C. S., *A&A*, 323:L49–L52, July 1997.

Petigura, E. A., Crossfield, I. J. M., Isaacson, H., Beichman, C. A., Christiansen, J. L., Dressing, C. D., Fulton, B. J., Howard, A. W., Kosiarek, M. R., Lépine, S., Schlieder, J. E., Sinukoff, E., & Yee, S. W., *AJ*, 155:21, January 2018.

Pollacco, D. L., Skillen, I., Collier Cameron, A., Christian, D. J., Hellier, C., Irwin, J., Lister, T. A., Street, R. A., West, R. G., Anderson, D. R., Clarkson, W. I., Deeg, H., Enoch, B., Evans, A., Fitzsimmons, A., Haswell, C. A., Hodgkin, S., Horne, K., Kane, S. R., Keenan, F. P., Maxted, P. F. L., Norton, A. J., Osborne, J., Parley, N. R., Ryans, R. S. I., Smalley, B., Wheatley, P. J., & Wilson, D. M., *PASP*, 118:1407–1418, October 2006.

Pope, B. J. S., Parviainen, H., & Aigrain, S., *MNRAS*, 461:3399–3409, October 2016.

Prisinzano, L., Micela, G., Sciortino, S., Affer, L., & Damiani, F., *A&A*, 546:A9, October 2012.

Prša, A., Harmanec, P., Torres, G., Mamajek, E., Asplund, M., Capitaine, N., Christensen-Dalsgaard, J., Depagne, É., Haberreiter, M., Hekker, S., Hilton, J., Kopp, G., Kostov, V., Kurtz, D. W., Laskar, J., Mason, B. D., Milone, E. F., Montgomery, M., Richards, M., Schmutz, W., Schou, J., & Stewart, S. G., *AJ*, 152:41, August 2016.

Queloz, D., Mayor, M., Udry, S., Burnet, M., Carrier, F., Eggenberger, A., Naef, D., Santos, N., Pepe, F., Rupprecht, G., Avila, G., Baeza, F., Benz, W., Bertaux, J.-L., Bouchy, F., Cavadore, C., Delabre, B., Eckert, W., Fischer, J., Fleury, M., Gilliotte, A., Goyak, D., Guzman, J. C., Kohler, D., Lacroix, D., Lizon, J.-L., Megevand, D., Sivan, J.-P., Sosnowska, D., & Weilenmann, U., *The Messenger*, 105:1–7, September 2001.

Rauer, H., Catala, C., Aerts, C., Appourchaux, T., Benz, W., Brandeker, A., Christensen-Dalsgaard, J., Deleuil, M., Gizon, L., Goupil, M.-J., Güdel, M., Janot-Pacheco, E., Mas-Hesse, M., Pagano, I., Piotto, G., Pollacco, D., Santos, Ċ., Smith, A., Suárez, J.-C., Szabó, R., Udry, S., Adibekyan, V., Alibert, Y., Almenara, J.-M., Amaro-Seoane, P., Eiff, M. A.-v., Asplund, M., Antonello, E., Barnes, S., Baudin, F., Belkacem, K., Bergemann, M., Bihain, G., Birch, A. C., Bonfils, X., Boisse, I., Bonomo, A. S., Borsa, F., Brandão, I. M., Brocato, E., Brun, S., Burleigh, M., Burston, R., Cabrera, J., Cassisi, S., Chaplin, W., Charpinet, S., Chiappini, C., Church, R. P., Csizmadia, S., Cunha, M., Damasso, M., Davies, M. B., Deeg, H. J., Díaz, R. F., Dreizler, S.,

Dreyer, C., Eggenberger, P., Ehrenreich, D., Eigmüller, P., Erikson, A., Farmer, R., Feltzing, S., de Oliveira Fialho, F., Figueira, P., Forveille, T., Fridlund, M., García, R. A., Giommi, P., Giuffrida, G., Godolt, M., Gomes da Silva, J., Granzer, T., Grenfell, J. L., Grotsch-Noels, A., Günther, E., Haswell, C. A., Hatzes, A. P., Hébrard, G., Hekker, S., Helled, R., Heng, K., Jenkins, J. M., Johansen, A., Khodachenko, M. L., Kislyakova, K. G., Kley, W., Kolb, U., Krivova, N., Kupka, F., Lammer, H., Lanza, A. F., Lebreton, Y., Magrin, D., Marcos-Arenal, P., Marrese, P. M., Marques, J. P., Martins, J., Mathis, S., Mathur, S., Messina, S., Miglio, A., Montalban, J., Montalto, M., Monteiro, M. J. P. F. G., Moradi, H., Moravveji, E., Mordasini, C., Morel, T., Mortier, A., Nascimbeni, V., Nelson, R. P., Nielsen, M. B., Noack, L., Norton, A. J., Ofir, A., Oshagh, M., Ouazzani, R.-M., Pápics, P., Parro, V. C., Petit, P., Plez, B., Poretti, E., Quirrenbach, A., Ragazzoni, R., Raimondo, G., Rainer, M., Reese, D. R., Redmer, R., Reffert, S., Rojas-Ayala, B., Roxburgh, I. W., Salmon, S., Santerne, A., Schneider, J., Schou, J., Schuh, S., Schunker, H., Silva-Valio, A., Silvotti, R., Skillen, I., Snellen, I., Sohl, F., Sousa, S. G., Sozzetti, A., Stello, D., Strassmeier, K. G., Švanda, M., Szabó, G. M., Tkachenko, A., Valencia, D., Van Grootel, V., Vauclair, S. D., Ventura, P., Wagner, F. W., Walton, N. A., Weingrill, J., Werner, S. C., Wheatley, P. J., & Zwintz, K., *Experimental Astronomy*, 38:249–330, November 2014.

Ricker, G. R., Latham, D. W., Vanderspek, R. K., Ennico, K. A., Bakos, G., Brown, T. M., Burgasser, A. J., Charbonneau, D., Deming, L. D., Doty, J. P., Dunham, E. W., Elliot, J. L., Holman, M. J., Ida, S., Jenkins, J. M., Jernigan, J. G., Kawai, N., Laughlin, G. P., Lissauer, J. J., Martel, F., Sasselov, D. D., Schingler, R. H., Seager, S., Torres, G., Udry, S., Villasenor, J. S., Winn, J. N., & Worden, S. P. *The Transiting Exoplanet Survey Satellite (TESS)*. In *American Astronomical Society Meeting Abstracts #213*, volume 41 of *Bulletin of the American Astronomical Society*, page 193, January 2009.

Rodriguez, J. E., Becker, J. C., Eastman, J. D., Hadden, S., Vanderburg, A., Khain, T., Quinn, S. N., Mayo, A., Dressing, C. D., Schlieder, J. E., Ciardi, D. R., Latham, D. W., Rappaport, S., Adams, F. C., Berlind, P., Bieryla, A., Calkins, M. L., Esquerdo, G. A.,

Kristiansen, M. H., Omohundro, M., Schwengeler, H. M., Stassun, K. G., & Terentev, I., *ArXiv e-prints*, June 2018.

Rojas-Ayala, B., Iglesias, D., Minniti, D., Saito, R. K., & Surot, F., *A&A*, 571:A36, November 2014.

Ryu, Y.-H., Udalski, A., Yee, J. C., Albrow, M. D., Chung, S.-J., Gould, A., Han, C., Hwang, K.-H., Jung, Y. K., Shin, I.-G., Zhu, W., Cha, S.-M., Kim, D.-J., Kim, H.-W., Kim, S.-L., Lee, C.-U., Lee, Y., Park, B.-G., Pogge, R. W., KMTNet Collaboration, Pietrukowicz, P., Kozłowski, S., Poleski, R., Skowron, J., Mróz, P., Szymański, M. K., Soszyński, I., Pawlak, M., Ulaczyk, K., & OGLE Collaboration, *AJ*, 154:247, December 2017.

Safonova, M., Mkrtichian, D., Hasan, P., Sutaria, F., Brosch, N., Gorbikov, E., & Joseph, P., *AJ*, 151:27, February 2016.

Saito, R. K., Hempel, M., Minniti, D., Lucas, P. W., Rejkuba, M., Toledo, I., Gonzalez, O. A., Alonso-García, J., Irwin, M. J., Gonzalez-Solares, E., Hodgkin, S. T., Lewis, J. R., Cross, N., Ivanov, V. D., Kerins, E., Emerson, J. P., Soto, M., Amôres, E. B., Gurovich, S., Dékány, I., Angeloni, R., Beamin, J. C., Catelan, M., Padilla, N., Zoccali, M., Pietrukowicz, P., Moni Bidin, C., Mauro, F., Geisler, D., Folkes, S. L., Sale, S. E., Borissova, J., Kurtev, R., Ahumada, A. V., Alonso, M. V., Adamson, A., Arias, J. I., Bandyopadhyay, R. M., Barbá, R. H., Barbuy, B., Baume, G. L., Bedin, L. R., Bellini, A., Benjamin, R., Bica, E., Bonatto, C., Bronfman, L., Carraro, G., Chenè, A. N., Clariá, J. J., Clarke, J. R. A., Contreras, C., Corvillón, A., de Grijs, R., Dias, B., Drew, J. E., Fariña, C., Feinstein, C., Fernández-Lajús, E., Gamen, R. C., Gieren, W., Goldman, B., González-Fernández, C., Grand, R. J. J., Gunthardt, G., Hambly, N. C., Hanson, M. M., Hełminiak, K. G., Hoare, M. G., Huckvale, L., Jordán, A., Kinemuchi, K., Longmore, A., López-Corredoira, M., Maccarone, T., Majaess, D., Martín, E. L., Masetti, N., Mennickent, R. E., Mirabel, I. F., Monaco, L., Morelli, L., Motta, V., Palma, T., Parisi, M. C., Parker, Q., Peñaloza, F., Pietrzyński, G., Pignata, G., Popescu,

B., Read, M. A., Rojas, A., Roman-Lopes, A., Ruiz, M. T., Saviane, I., Schreiber, M. R., Schröder, A. C., Sharma, S., Smith, M. D., Sodré, L., Stead, J., Stephens, A. W., Tamura, M., Tappert, C., Thompson, M. A., Valenti, E., Vanzi, L., Walton, N. A., Weidmann, W., & Zijlstra, A., *A&A*, 537:A107, January 2012.

Saviane, I., Da Costa, G. S., Held, E. V., Sommariva, V., Gullieuszik, M., Barbuy, B., & Ortolani, S., *A&A*, 540:A27, April 2012.

Scargle, J. D., *ApJ*, 263:835–853, December 1982.

Schlegel, D. J., Finkbeiner, D. P., & Davis, M., *ApJ*, 500:525–553, June 1998.

Schlieder, J. E., Crossfield, I. J. M., Petigura, E. A., Howard, A. W., Aller, K. M., Sinukoff, E., Isaacson, H. T., Fulton, B. J., Ciardi, D. R., Bonnefoy, M., Ziegler, C., Morton, T. D., Lépine, S., Obermeier, C., Liu, M. C., Bailey, V. P., Baranec, C., Beichman, C. A., Defrère, D., Henning, T., Hinz, P., Law, N., Riddle, R., & Skemer, A., *ApJ*, 818:87, February 2016.

Seager, S. & Mallén-Ornelas, G., *ApJ*, 585:1038–1055, March 2003.

Shao, M. & Colavita, M. M., *ARA&A*, 30:457–498, 1992.

Sinukoff, E., Howard, A. W., Petigura, E. A., Schlieder, J. E., Crossfield, I. J. M., Ciardi, D. R., Fulton, B. J., Isaacson, H., Aller, K. M., Baranec, C., Beichman, C. A., Hansen, B. M. S., Knutson, H. A., Law, N. M., Liu, M. C., Riddle, R., & Dressing, C. D., *ApJ*, 827:78, August 2016.

Stellingwerf, R. F., *ApJ*, 224:953–960, September 1978.

Sung, H., Chun, M.-Y., & Bessell, M. S., *AJ*, 120:333–348, July 2000.

Tsapras, Y., Arellano Ferro, A., Bramich, D. M., Jaimes, R. F., Kains, N., Street, R., Hundertmark, M., Horne, K., Dominik, M., & Snodgrass, C., *MNRAS*, 465:2489–2504, February 2017.

Udalski, A., Szymanski, M., Kaluzny, J., Kubiak, M., & Mateo, M., , 42:253–284, 1992.

Van Eylen, V., Nowak, G., Albrecht, S., Palle, E., Ribas, I., Bruntt, H., Perger, M., Gandolfi, D., Hirano, T., Sanchis-Ojeda, R., Kiilerich, A., Prieto-Arranz, J., Badenas, M., Dai, F., Deeg, H. J., Guenther, E. W., Montañés-Rodríguez, P., Narita, N., Rogers, L. A., Béjar, V. J. S., Shrotriya, T. S., Winn, J. N., & Sebastian, D., *ApJ*, 820:56, March 2016.

Vanderburg, A. & Johnson, J. A., *PASP*, 126:948, October 2014.

Vanderburg, A., Latham, D. W., Buchhave, L. A., Bieryla, A., Berlind, P., Calkins, M. L., Esquerdo, G. A., Welsh, S., & Johnson, J. A., *ApJS*, 222:14, January 2016.

Wittenmyer, R. A., Sharma, S., Stello, D., Buder, S., Kos, J., Asplund, M., Duong, L., Lin, J., Lind, K., Ness, M., Zwitter, T., Horner, J., Clark, J., Kane, S. R., Huber, D., Bland-Hawthorn, J., Casey, A. R., De Silva, G. M., DOrazi, V., Freeman, K., Martell, S., Simpson, J. D., Zucker, D. B., Anguiano, B., Casagrande, L., Esdaile, J., Hon, M., Ireland, M., Kafle, P. R., Khanna, S., Marshall, J. P., Saddon, M. H. M., Traven, G., & Wright, D., *AJ*, 155:84, February 2018.

Yu, L., Crossfield, I. J. M., Schlieder, J. E., Kosiarek, M. R., Feinstein, A. D., Livingston, J. H., Howard, A. W., Benneke, B., Petigura, E. A., Bristow, M., Christiansen, J. L., Ciardi, D. R., Crepp, J. R., Dressing, C. D., Fulton, B. J., Gonzales, E. J., Hardegree-Ullman, K. K., Henning, T., Isaacson, H., Lépine, S., Martinez, A. O., Morales, F. Y., & Sinukoff, E., *AJ*, 156:22, July 2018.

Zacharias, N., Monet, D. G., Levine, S. E., Urban, S. E., Gaume, R., & Wycoff, G. L., *VizieR Online Data Catalog*, 1297, November 2005.

Zacharias, N., Finch, C. T., Girard, T. M., Henden, A., Bartlett, J. L., Monet, D. G., & Zacharias, M. I., *VizieR Online Data Catalog*, 1322, July 2012.

Zechmeister, M. & Kürster, M., *A&A*, 496:577–584, March 2009.

Zhu, W., Huang, C. X., Udalski, A., Soares-Furtado, M., Poleski, R., Skowron, J., Mróz, P., Szymański, M. K., Soszyński, I., Pietrukowicz, P., KozŁowski, S., Ulaczyk, K., & Pawlak, M., *PASP*, 129(10):104501, October 2017.

Zoccali, M. & Valenti, E., *pasa*, 33:e025, June 2016.

Zoccali, M., Hill, V., Lecureur, A., Barbuy, B., Renzini, A., Minniti, D., Gómez, A., & Ortolani, S., *A&A*, 486:177–189, July 2008.